REPORT DOCUMENTATION PAGE

Form Approved
OMB No. 074-0188

Public reporting burden for this collection of information is estimated to average 1 hour per response, including the time for reviewing instructions, searching existing data sources, gathering and maintaining the data needed, and completing and reviewing this collection of information. Send comments regarding this burden estimate or any other aspect of this collection of information, including suggestions for reducing this burden to Washington Headquarters Services, Directorate for Information Operations and Reports, 1215 Jefferson Davis Highway, Suite 1204, Arlington, VA 22202-4302, and to the Office of Management and Budget, Paperwork Reduction Project (0704-0188), Washington, DC 20503

1. AGENCY USE ONLY (Leave blank)	2. REPORT DATE	3. REPORT TYPE AND DATES COVERED
	Jan 4, 2001	

4. TITLE AND SUBTITLE

Mechanical and Microstructural Analysis on the High Temperature Deformation of Gamma TiAl Alloy

5. FUNDING NUMBERS

AOARD-99-4009

6. AUTHOR(S)

Jeoung Han Kim and Chong Soo Lee

7. PERFORMING ORGANIZATION NAME(S) AND ADDRESS(ES)

Pohang University of Science and Technology

San 31, Hyoja-dong,
Pohang
790-784, KOREA

8. PERFORMING ORGANIZATION REPORT NUMBER

9. SPONSORING / MONITORING AGENCY NAME(S) AND ADDRESS(ES)

Asian Office of Aerospace Research and Development
7-23-17 Roppongi
Minato-ku, Tokyo 106-0032
Tel:+81-3-5410-4409 Fax:+81-3-5410-4407

10. SPONSORING / MONITORING AGENCY REPORT NUMBER

11. SUPPLEMENTARY NOTES

20010124 162

12a. DISTRIBUTION / AVAILABILITY STATEMENT

DISTRIBUTION STATEMENT A
Approved for Public Release
Distribution Unlimited

12b. DISTRIBUTION CODE

13. ABSTRACT

It is aimed in this study to investigate the high temperature deformation mechanisms of two-phase gamma TiAl alloy in view of the inelastic deformation theory and to quantify the relative contribution of each mechanism to the overall deformation. The influence of γ/α_2 volume fraction on high temperature deformation behavior and the preferable cavity initiation sites have also been studied. For this purpose, a series of load relaxation tests and tensile tests have been conducted at temperatures ranging from 800 to 1050°C.

In the early stage of the deformation, (as in the load relaxation test) flow curves of the fine-grained TiAl alloy are well fitted with the combined curves of grain matrix deformation and dislocation climb. The evidence of grain boundary sliding has not been observed. However, when the amount of deformation is large (exceeding 80%), flow curves changes its shape indicating that other deformation mechanism operates at this stage. It is identified as grain boundary sliding resulted from dynamic recrystallization.

The activation energy values for grain matrix deformation and dislocation climb have been obtained from constitutive parameters analysis. Calculated values for Q_{GMD} and $Q_{disl.\ climb}$ are 319kJ/mol and 386 kJ/mol, respectively. $Q_{disl.\ climb}$ is found to be similar to that for self-diffusion of Al in TiAl or in Ti_3Al.

With the increase in the volume fraction of α_2-phase, the flow stress for grain matrix deformation increases because α_2-phase is considered as hard phase which acts as barrier for dislocation movement. The fact that the frequency of cavity initiation at α_2/γ is 8 times as high as that of γ/γ, supports the above interpretation.

14. SUBJECT TERMS			15. NUMBER OF PAGES 70
			16. PRICE CODE
17. SECURITY CLASSIFICATION OF REPORT	18. SECURITY CLASSIFICATION OF THIS PAGE	19. SECURITY CLASSIFICATION OF ABSTRACT	20. LIMITATION OF ABSTRACT

NSN 7540-01-280-5500

DTIC QUALITY INSPECTED 4

Standard Form 298 (Rev. 2-89)
Prescribed by ANSI Std. Z39-18
298-102

A Research Report to AFOSR/AOARD

MECHANICAL AND MICROSTRUCTURAL ANALYSIS ON THE HIGH TEMPERATURE DEFORMATION OF GAMMA TiAl ALLOY

by

Jeoung Han Kim and Chong Soo Lee
Center for Advanced Aerospace Materials
Department of Materials Science and Engineering
Pohang University of Science and Technology
Pohang 790-784, KOREA

Jan 4, 2001

Abstract

It is aimed in this study to investigate the high temperature deformation mechanisms of two-phase gamma TiAl alloy in view of the inelastic deformation theory and to quantify the relative contribution of each mechanism to the overall deformation. The influence of γ/α_2 volume fraction on high temperature deformation behavior and the preferable cavity initiation sites have also been studied. For this purpose, a series of load relaxation tests and tensile tests have been conducted at temperatures ranging from 800 to 1050°C.

In the early stage of the deformation, (as in the load relaxation test) flow curves of the fine-grained TiAl alloy are well fitted with the combined curves of grain matrix deformation and dislocation climb. The evidence of grain boundary sliding has not been observed. However, when the amount of deformation is large (exceeding 80%), flow curves changes its shape indicating that other deformation mechanism operates at this stage. It is identified as grain boundary sliding resulted from dynamic recrystallization.

The activation energy values for grain matrix deformation and dislocation climb have been obtained from constitutive parameters analysis. Calculated values for Q_{GMD} and $Q_{disl.\ climb}$ are 319kJ/mol and 386 kJ/mol, respectively. $Q_{disl.\ climb}$ is found to be similar to that for self-diffusion of Al in TiAl or in Ti_3Al.

With the increase in the volume fraction of α_2-phase, the flow stress for grain matrix deformation increases because α_2-phase is considered as hard phase which acts as barrier for dislocation movement. The fact that the frequency of cavity initiation at α_2/γ is 8 times as high as that of γ/γ, supports the above interpretation.

Contents

1. Introduction

During the past several decades, a considerable research effort has been made in the aerospace industry to develop high temperature structural materials that combine low density with high-temperature strength for application of engine components. This research has led to titanium-aluminum alloys based on the γ-TiAl phase because of their high strength-to-weight ratio, high Young's moduli, and good oxidation resistance [1,2]. γ-TiAl alloys also exhibit high strength and creep resistance at temperatures up to 1073 K, associated with a high activation energy for diffusion. This high-energy barrier is originated from the nature of strong Ti-Al bond. However, this rigid bond structure leads to a limited number of available slip systems. As a result, this material exhibits brittle fracture and poor ductility, which prevents so far commercial applications of these alloys. Accordingly, many investigations have been focused to find the source of brittleness and to enhance the ductility and hot workability by the addition of other alloying elements and/or by the control of microstructure [3-7]. The superplastic forming method, one of a novel processing techniques, is known to be an efficient and cost-saving method to produce complex components from these difficult-to-fabricate materials. While most of studies have concentrated to enhance the superplasticity of two phase γ-TiAl alloy [8-11], only limited information on high temperature mechanisms are available and there still remain several vague points.

First, what are the predominant deformation mechanisms operating at high temperatures? Also it is questioned as to the relative contribution of each mechanism to overall deformation. There are several high temperature deformation mechanisms such as grain matrix deformation, dislocation creep and grain boundary sliding [12-14]. Until

now, however, several efforts have been made to understand each mechanism using power law relationship. However, this approach provides only the phenomenological description of high temperature deformation behavior lacking fundamental understanding for the material behavior.

Second, since it is important to determine the deformation behavior should be clarified. In practical situation, it is important to determine the optimum volume ratio showing the best mechanical properties in two-phase alloys. In earlier investigation on Ti-6Al-4V alloy, the largest elongation is observed in the 50% α/β structure due to the lowest sliding resistance of α/β boundaries, and in $20\alpha_2 / 80\beta$ structure in Ti_3Al alloy [15-16]. It is of great worth to investigate the influence of γ/α_2 volume fraction on high temperature deformation of γ-TiAl alloy.

Third, cavity initiation mechanisms and preferred sites are not clearly known. This information is important in optimizing the microstructure for best hot working performance [17-18].

To investigate the aforementioned points, high temperature deformation characteristics of γ-TiAl alloy have been analyzed in view of inelastic deformation theory [19] and microstructure observation. To generate a proper relationship between stress and strain rate, load relaxation tests representing minimal microstructural change have been conducted at elevated temperatures. The deformed microstructures are also investigated by scanning and transmission electron microscopy to understand the prevailing deformation mode at high temperatures.

2. Literature review

2.1. A physical characteristics of gamma-TiAl alloys

2.1.1. Mechanical properties

γ-TiAl is an ordered intermetallic compound of the lightweight elements Ti and Al. Its low density, which is less than half of that of superalloys, is an important attribute for gas turbine engine applications. Lightweight materials increase the engine performance as measured by thrust-to-weight ratio. The benefit can be more than pound for pound savings, since the use of a lightweight rotating part frequently reduces the dimensions of the stress-supporting structures. Additionally, the high aluminum content of this compound increases the resistance to oxidation and burning, two critical concerns in the use of titanium-based materials.

Property	α_2 alloys	γ alloys	Superalloys
Density (g cm^{-3})	4.1 –4.7	3.8-4.0	8.3
Young's modulous (GPA)	120-145	160-175	206
Ductility (%)	2-5	1-3	3-5
Yield strength (Mpa)	700-900	400-650	1100
Thermal conductivity (W $m^{-1} K^{-1}$)	7	22	11
Phase stability limit (°C)	1180	1440	1450
Creep limit (°C)	750	900	1090
Oxidation limit (°C)	650	900	1090

TABLE 1. Properties of titanium aluminide alloys and superalloys [5]

γ-TiAl remains ordered to melting at ~1440°C. The strong Ti-Al bond leads to a high activation energy for diffusion. This high-energy barrier helps to retain strength

and resist creep to high temperatures when diffusion becomes the rate-controlling process. It also results in high stiffness over a wide temperature range making possible its use for static parts that need only to sustain elastic deflection [20]. However, the rigid bond structure restricts the ability to accommodate plastic deformation. As with most other intermetallic compounds, γ, without modification, lacks the ductility and toughness that are necessary for structural application. Its high thermal conductivity allows easier cooling of hot parts. Some properties of titanium aluminide alloy and superalloys are shown in Table 1.

2.1.2. Phase Diagrams

The central portion of the Ti-Al phase diagram was controversial for nearly 40 years before the currently accepted version was constructed. This version, depicted in Fig. 1, shows three solid phases (γ-TiAl, α_2-Ti_3Al and high-temperature α-Ti) and two-phase reactions (a peritectic L + α →γ reaction and a eutectoid α→α_2 + γ reaction). While the precise location of the phase boundaries remains under investigation, a few additional features may be noted. The alpha-2 phase with the $D0_{19}$ (ordered hexagonal) structure has a composition that can vary between 48.5 at.% Al and 66 at.% Al depending upon temperature, and it remains ordered up to its melting point of ~1,450°C. For the stoichiometric compound, c/a=1.015; this tetragonality ratio increase to 1.03 with increasing aluminum concentration and decreases to 1.01 with decreasing aluminum atom[21-23]. At off-stoichiometric composition, excess titanium or aluminum atoms occupy opposite anti-sites without creating vacancies. When the gamma phase is precipitated out of either the alpha matrix, these phases have the crystallographic orientation relationship of (111)||(0002) and [110]||[1120]. Ternary phase diagrams are

available for several Tl-Al-M systems; however, only the Ti-Al-Nb system has been studied relatively extensively [24,25]. These ternary diagrams can be classified into three types depending on the direction of the gamma phase field. Precise placements of phase boundaries, however, await more careful measurements even in the Ti-Al-Nb system.

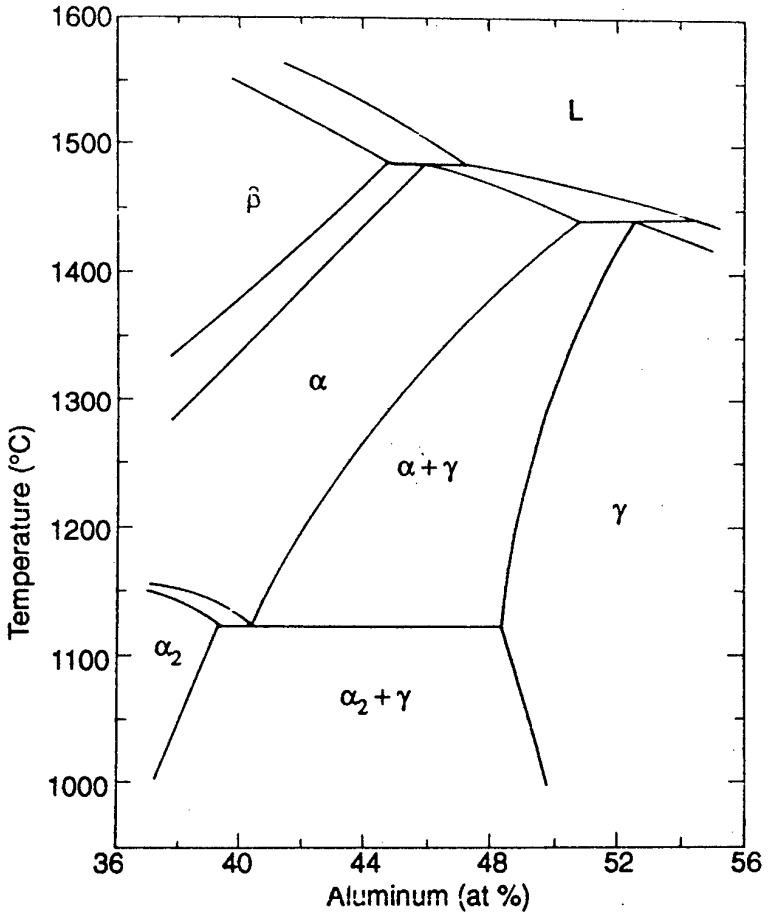

Fig 1. A partial Ti-Al phase diagram near the stoichiometric TiAl composition [29]

2.1.3. Factors Controlling Ductility

The ductility of gamma alloys is controlled by alloy chemistry and microstructure. Studies on Ti-(43-55)Al compositions showed that the lowest strength occurs at

compositions around Ti-51Al and that room-temperature elongation varies with aluminum content, exhibiting a maximum centered around the two-phase composition of Ti-48Al [26,27]. The decreased ductility with increasing aluminum content in the single-phase region was attributed to the increased tetragonality ratio and increased covalent bonding or decreased metallic bonding [28].

Additions of vanadium, chromium or manganese increase the ductility of two-phase gamma alloys but have no obvious effect in single-phase alloys containing more than 50 at.% Al. Small additions of these elements in two-phase gamma compositions are believed to increase metallic bonding by decreasing aluminum content in the gamma phase [29,30]. For a given two-phase alloy composition, microstructural variations directly influence the room-temperature tensile ductility, which ranges from 0.5% to 3.5% plastic elongation. Consequently, the specific role of a particular alloying element is not yet established, since both intrinsic changes in the properties of the phases and changes in the microstructures result from a given process applied to different alloys. Detailed studies are required to establish these effects.

Interstitial impurities such as oxygen, nitrogen, carbon, and boron reduce the ductility significantly when their total concentration exceeds roughly 0.1 wt.%[29]. For example, Ti-48Al with a duplex microstructure exhibits a room-temperature tensile ductility of 2% with 800ppm oxygen and 2.7% with 370ppm oxygen. There has been speculation that the alpha-2 phase or the addition of erbium can scavenge oxygen in the gamma phase, thereby increasing the purity and thus the ductility of the gamma phase. Scavenging has been observed macroscopically Ti-47Al and Ti-51Al containing 1.1 wt.% oxygen.

2.1.4 Deformation Mechanisms

The arrangement of titanium and aluminum atoms in layers on successive (002) planes in the gamma $L1_0$ structure results in ordinary dislocations having b= 1/2<110], and superdislocations with b=<011] and 1/2 <112], on {111} planes [31,32]. The superdislocations are extended to produce planar faults such as stacking faults and antiphase boundaries. Single-phase gamma alloys[Ti-(50-56)Al] have very low room-temperature ductility, and both ordinary and superdislocations exhibit sessile components. This is believed to be due to a large Peierls stress, and extrinsically faulted dipoles, respectively. With decreasing aluminum content, the ordinary dislocation activity increases and twining is possibly promoted by the increased 1/2<112] mobility [33,34]. Single Crystalline TiAl exhibits a flow stress anomaly, with the peak stress at about 600°C. This has been interpreted as being the result of the cross-slip of <101] dislocations from {111} to {100} creating a sessile defect, but several inconsistencies in this mechanism remain to be clarified.

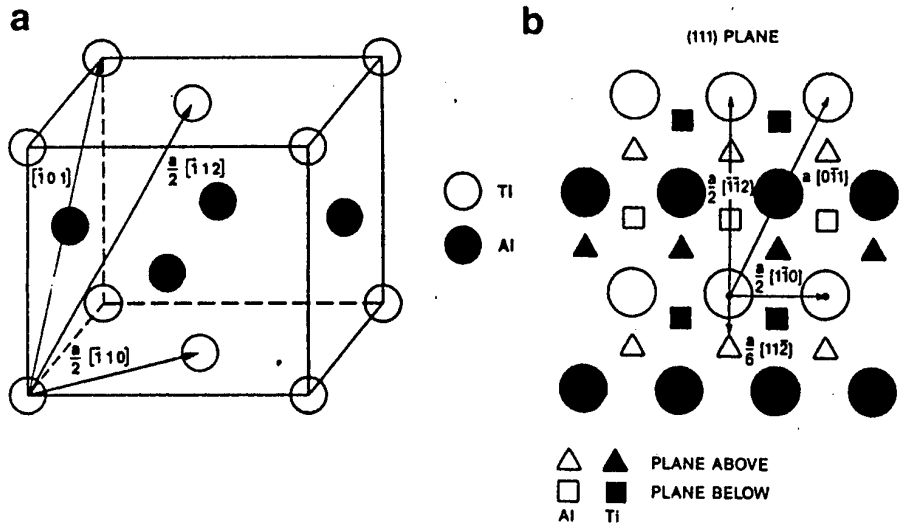

Fig. 2. (a) Ordered face-centered tetragonal ($L1_0$) TiAl structures and (b) slip dislocations on the (111) plane [29]

In two-phase Ti-(47-49)Al binary alloys with duplex microstructures, the deformation of the gamma phase takes place by ordinary dislocation activity and microtwinning associated with 1/6<112] partials. Above the brittle-to-ductile transition temperature (around 700°C), deformation takes place predominantly by ordinary dislocation slip and also microtwinning as in single-phase alloys [33,35]. The addition of chromium,vanadium or manganese was shown to increase both slip and twinning activity in gamma alloys having the duplex microstructure. In fully lamellar structures, a very low dislocation activity and almost no twinning activity were observed. The reason for this is unknown and only serves to show that while several studies of deformation mechanisms have been performed, many aspects remain controversial and await more detailed study [36].

2.1.5. Microstructural Types

With the aid of the phase diagram in Fig.1, it can describe various microstructures obtainable in TiAl-based materials. The classification here is primarily based on phase equilibria as a function of heat treatment temperature and alloy composition. The microstructural size scale is also a function of heat treatment time and cooling schedule, and only typical values are given below for comparison. The structures here can be readily obtained by rapid solidification or wrought processing of ingots. These processing approaches break up the solidification structure and achieve homogeneity and grain refinement through rapid solidification or work-induced recrystallization. In conventionally cast materials, the solidification structure does not respond to heat treatment as readily. It generally remains coarse and inhomogeneous after annealing, but the same microstructural classification still applies.

As a result of the solid-state phase equilibria shown in Fig. 1, three distinctly

different types of microstructures can be obtained by annealing [37]. These are shown in Fig. 3. Alloys above 52 at.% Al generally lie in the single-phase γ field during heat treatment, and are single-phase γ after cooling to room temperature (Fig. 3a). The grains are equiaxed and about 50μm in diameter. For alloys between 46 and 50 at.%Al, heat treatment in the $\alpha+\gamma$ phase field results in a two-phase structure upon cooling (Fig. 3b). This structure consists of γ grains and grains of a lamellar structure. The lamellar grains contain alternating α_2 and γ plates, which form as a result of transformation from the primary α during cooling to room temperature. The grains are typically 10-35μm in diameter, and the lamellar plates are 0.1-1μm thick. This structure is referred to as the duplex structure. Finally, alloys below 48 at.%Al that are heat treated in the single-phase α filed can form the fully lamellar structure, as shown in Fig. 3(d). The grains are typically greater than 500μm in diameter, which reflects the rapid coarsening rate of the disordered α.

Additional microstructures that are variations of the above can be obtained [26]. For the duplex structure, the volume ratio between the transformed α and primary γ increases with heat treatment temperature. If a composition is heat treated at a temperature only slightly above the γ solvus, a small fraction of α will form at grain boundaries or triple points. These small α particles will still retard the growth of the γ grains, but they tend just to order into α_2 rather than transformation into the two-phase lamellar structure. This structure is referred to as the supersolvus structure. On the other hand, if the heat treatment is done at a temperature just below the α transus, a structure consisting of large transformed grains that are dispersed with small islands of undissolved γ may be obtained. This structure is referred to as the subtransus structure. Additionally, an equiaxed structure consisting of single-phase γ grains and single-phase

α_2 grains may be obtained by a long-time aging in the $\alpha_2+\gamma$ phase field below the eutectoid temperature. This structure is referred to as the dual-phase structure.

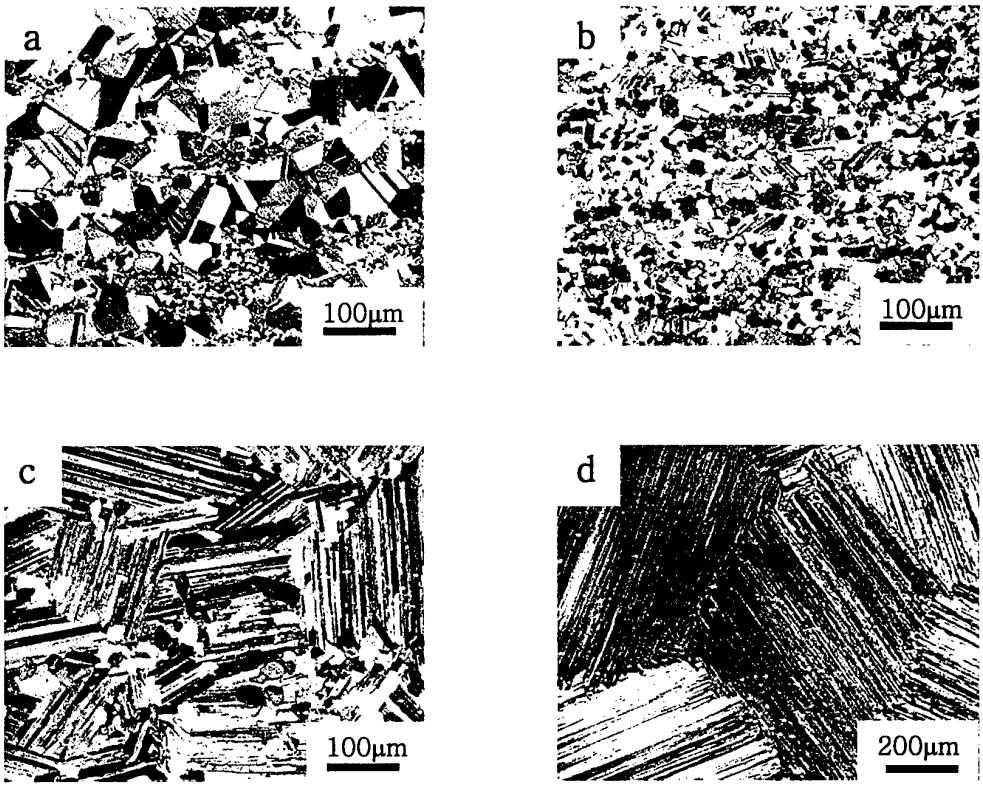

Fig. 3. Typical wrought microstructures of (a) near-gamma, (b) duplex, (c) nearly lamellar, (d) fully lamellar [36]

2.2. High Temperature Deformation Mechanisms of γ-TiAl

2.2.1. Phenomenological Deformation Behavior

Typical flow curve of high temperature deformation is shows as Fig. 4.

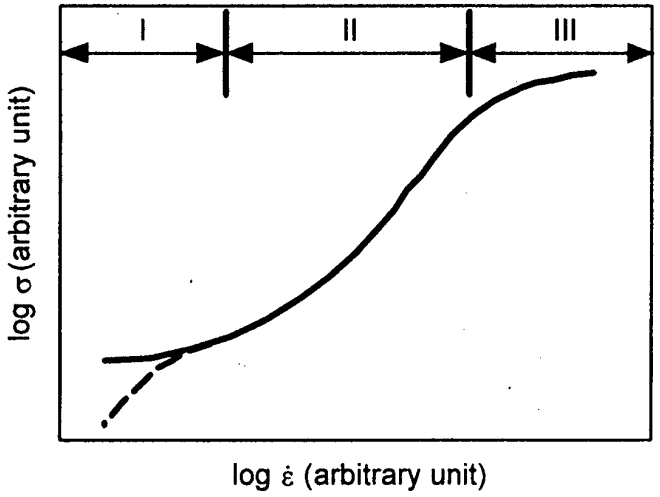

Fig. 4. Typical flow curve of high temperature deformation

The deformation behavior of crystalline materials has been described phenomenological by a power law relationship.

$$\sigma = K\dot{\varepsilon}^{m} \qquad (1)$$

The power a power index m is then naturally defined as the slope of logσ vs logε̇ curves and generally called the strain rate sensitivity parameter. This parameter has widely been used as a representative variable to characterize high temperature deformation behavior. It is, in general, believed that a large value of m is required for superplastic deformation, observed to vary continuously on log σ vs. logε̇ curve and furthermore there is no critical value of m, above which superplastic deformation can be predicted [38,39]. It is believed, in this regard, that the phenomemological power law relationship may not be a

suitable constitutive relationship for high temperature deformation.

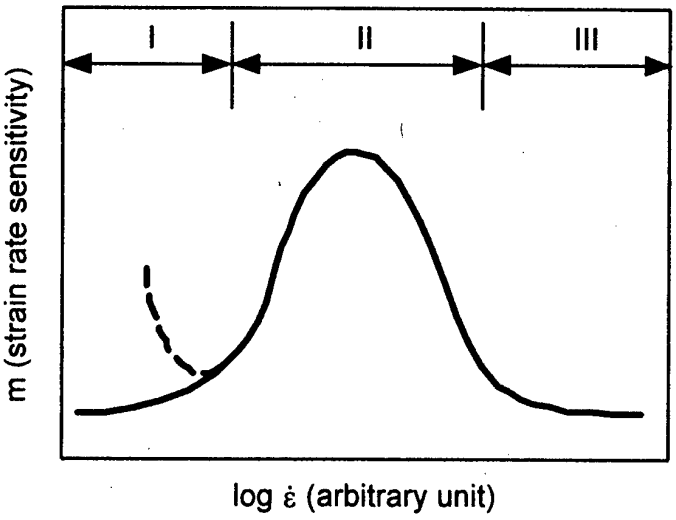

Fig. 5. Variation of strain rate sensitivity

There are two viewpoints on explanation of the region I as shown in straight and dot line. First, flow stress curve indicates critical stress value as like straight line and converge into the direction of log $\dot{\varepsilon}$. Second, if flow stress curve go below critical stress for grain boundary sliding, dislocation slip, which has relatively high deformation rate, dominates total deformation. And stress curves converge into the direction of log σ as like dot line [40,41]. The viewpoint of this study is corresponding to the latter one.

2.2.2. Grain boundary sliding

Grain boundary sliding is an important process in superplastic deformation such that, for several superplastic alloys [42]. However, if there is no change in shape of grain by an accommodation mechanism as shown in Fig. 6., microscopically it can't be avoided to voids initiation at triple point [43]. During actual deformation, such voids initiation inhibits to form large elongations and it can't be observable in microstructure observation before

large deformation. So the view of existence of accommodation mechanism is agreed with many researchers. However, there still remain many problems and unified theory on that is not available.

In explanation of accommodation mechanism for GBS, most phenomenological approach has divided into two ways that one has been made by taking diffusional accommodation the other by dislocation glide. However, in any case, both has been used deformation rate equation (2) and explained rate-determining mechanism according to each parameter that are obtained by flow curve analysis.

$$\dot{\varepsilon} \propto \frac{D}{kT}\left(\frac{b}{d}\right)^{q}\left(\frac{\sigma}{G}\right)^{n} \qquad (2)$$

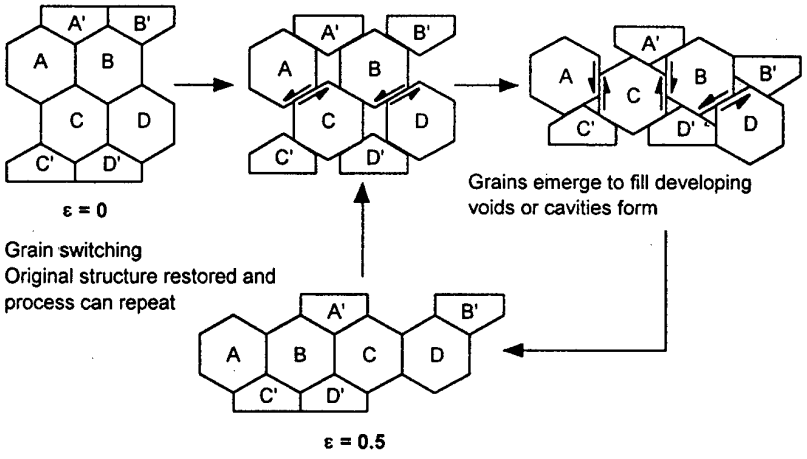

Fig. 6. GBS of the complete rigid system of grain [63]

2.2.2. Dynamic Recrystallization

When crystalline materials are deformed at elevated temperatures, the accumulated dislocations are continuously destroyed by two separate processes, The more common one, dynamic recovery, leads to the annihilation of pairs of dislocations, as well as to the

formation of subgrains and regular sub-boundaries. In high stacking fault energy materials, such recovery processes completely balance the effects of straining and of work hardening, leading to the establishment of steady state flow. By contrast, in materials of moderate to low fault energy, the dislocation density increases to appreciably higher levels; eventually the local differences in density are high enough to permit the nucleation of recrystallization during deformation (Fig. 7.). Such dynamic recrystallization leads to the elimination of large numbers of dislocations by the migration of high angel boundaries [44].

Dynamic recrystallization is usually encountered during hot deformation (or creep) of fcc metal and alloys with intermediate or low stacking-fault energies. It has also been observed in bcc metals of very high purity, e.g.,α-Fe. The experimental evidence for the occurrence of dynamic recrystallization has been furnished via examination of specimens quenched rapidly following hot deformation.

In order to initiate dynamic recrystallization, a critical deformation, ε_c, is necessary; that is somewhat less than ε(max). The corresponding stress, σ_c, is accordingly less than σ(max), but the low work-hardening rate in the vicinity of the peak renders these quantities virtually identical (Fig. 8.). Dynamic recrystallization of polycrystals is usually initiated at pre-existing grain boundaries. At very low $\dot{\varepsilon}$ and at large initial grain size, and of course for single crystals, intragranular nucleation becomes relatively more important. Apart form the very initial stages; the recrystallized grain size remains more or less constant during the reaction, with little or no grain growth proceeding simultaneously [45].

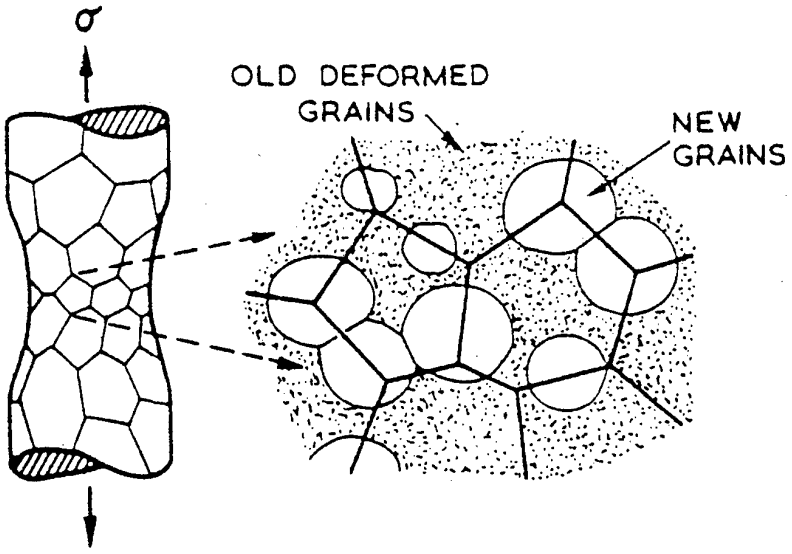

Fig. 7. Dynamic recrystallization replaces deformed by undeformed material [44]

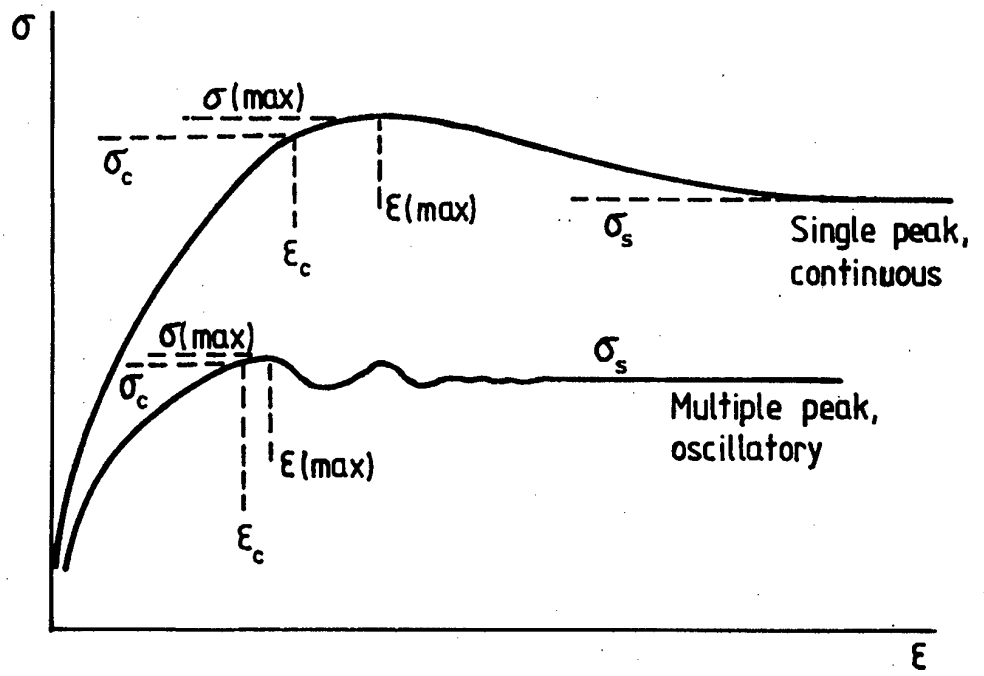

Fig. 8. Shape of σ-ε curves associated with high temperature deformation at constant strain rate [45]

2.2.3. Dislocation Climb Creep

At high temperature, dislocations acquire a new degree of freedom: they can climb as well as glide (Fig. 7.). If a gliding dislocation is held up by discrete obstacles, a little climb may release it, allowing it to glide to the next set of obstacle where the process is repeated. The glide step is responsible for almost all of the strain, although its average velocity is determined by the climb step. Mechanisms, which are based on this climb-plus-glide sequence, are referred to as climb-controlled creep [46-48]. The important feature which distinguishes these mechanisms from those of earlier sections is that the rate-controlling process, at an atomic level, is the diffusive motion of single ions or vacancies to or from the climbing dislocation, rather than the activated glide of the dislocation itself. Above $0.6T_m$ climb is generally lattice-diffusion controlled.

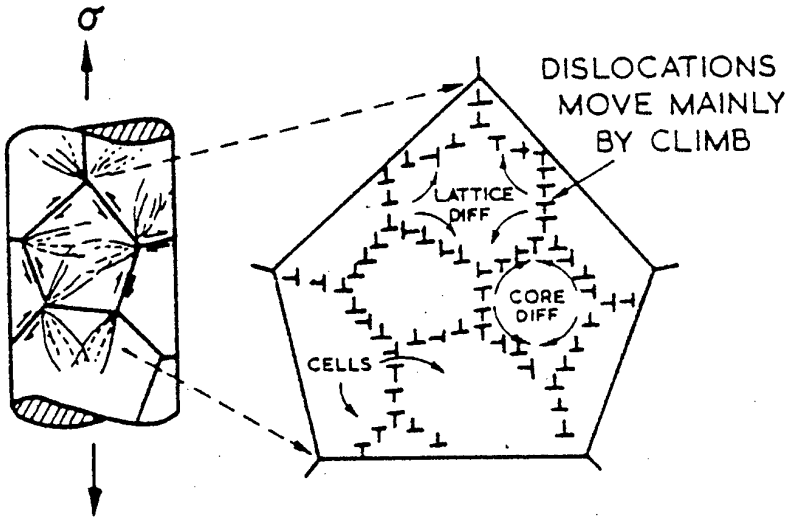

Fig. 7. Dislocation climb creep involving cell-formation by climb [44]

Some materials obey the equation (3) as followed: they exhibit proper-law creep with power of n and constant A_1 of about 1. However, present theoretical models for this behavior are unsatisfactory. None can convincingly explain the observed value of n; and

the large values of the dimensionless constant A_1 (up to 10^{15}) strongly suggest that some important physical quantity is missing from the equation in its present form. But it does provide a good description of experimental observation.

$$\dot{\gamma} = A_1 \frac{D_v \mu b}{kT} \left(\frac{\sigma_s}{\mu} \right)^n \qquad (3)$$

3. An inelastic deformation theory

The superplastic deformation behavior of crystalline materials has been described phenomenlogically by a power law relationship between the two external variable, *viz.* flow stress (σ) and strain rate ($\dot{\varepsilon}$), with power a power index *m*. The value of *m* is then naturally defined as the slope of logσ vs log$\dot{\varepsilon}$ curves and generally called the strain rate sensitivity parameter. This parameter has widely been used as a representative variable to characterize superplastic deformation behavior [49-51]. It is, in general, believed that a large value of *m* is required for superplastic deformation, observed to vary continuously on log σ vs log$\dot{\varepsilon}$ curve and furthermore there is no critical value of m, above which superplastic deformation can be predicted. It is believed, in this regard, that the phenomemological power law relationship may not be a suitable constitutive relationship for superplastic deformation. Therefore, it is attempted to formulate a new physically based superplasticity theory utilizing the concept of internal state variables [19] instead of the conventionally used external variables.

3.1.Dislocation kinematics

An elementary material volume *V* bounded by a surface S "within" and "across" which dislocations are allowed to move in response to an applied stress as in Fig.8 is considered. When the material boundary acts as a "barrier" partially blocking the passage of dislocation, some of them would remain inside the material volume giving rise to an internal strain. While at the same time the rest will pass through to produce an externally observable material deformation. These simultaneous processes of accumulation within *V* and the passage through S of dislocations are believed to be the most fundamental deformation mechanism responsible for various mechanical-

phenomena.

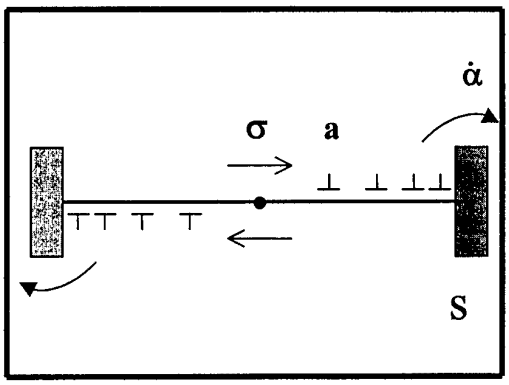

Fig.8. An internal variable model for inelastic deformation

To examine the internal deformation, the total inelastic deformation excluding the usual elastic part together with a possibly concurring rigid body rotation is conveniently assumed to occur in two successive steps as schematically depicted in Fig.9. The material volume is first regarded as fixed in the "external observer frame" (χ) to isolate the internal motion of dislocation. By assigning a "material reference frame" (ζ) attached to the material volume, the motion of dislocation is specified by a displacement vector λ from which the dislocation velocity ν can be defined as its material time rate. The two unit vectors **s** and **m** in Fig.9. are attached to the dislocation and thus represent the "internal observer frame" together with the unit line sense vector ***t***, tangent to the dislocation line. It is also noted that a general rotation of the dislocations is allowed in this process. Our attention here is focused on this internal deformation process occurring in the material volume V fixed in space as depicted in Fig.9(a).

Following the usual continuum approach for dislocation, the density distribution function $\rho(\zeta,t)$ is prescribed in reference to the material frame by

$$\frac{\partial \rho}{\partial \rho} = \nabla_{\zeta} \cdot (\rho v) = \rho \dot{c} \qquad (4)$$

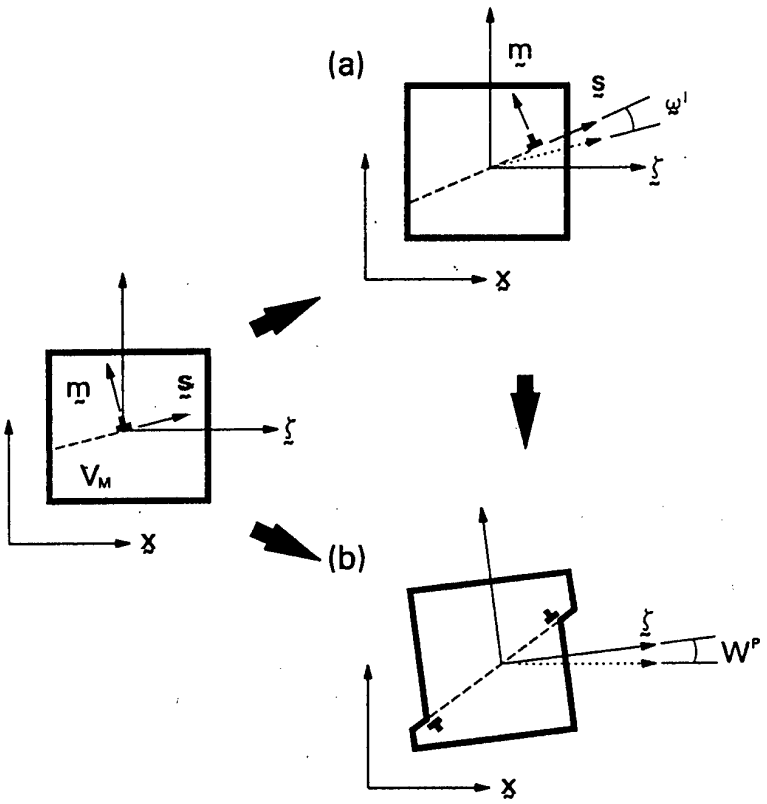

Fig.9. Dislocation motion in two successive stages: (a) internal motion produces internal distortion (β) and spin (ϖ^I); (b) dislocation flux across the material boundary generates non-recoverable deformation and plastic spin (W^P) [15]

including the production/annihilation rate term $\dot{c}$. The elementary material volume V is further taken in such a way that all of the dislocations within V have the same Burgers vector **b** and glide direction **s**. Since dislocation glide is a conservative motion producing material distortion, a symmetric internal distortion tensor can be defined by

$$\beta(\zeta,t) = b\rho\lambda M \qquad (5a)$$

$$M = \frac{1}{2}(sm + ms) \qquad (5b)$$

Here b denotes the magnitude of the burgers vector **b**, λ the glide distance parameter ($\lambda=\boldsymbol{\lambda}\cdot\mathbf{s}$) and **M** the glide orientation tensor. In this way, the variable has the unit of strain physically and represents the symmetric part of the internal distortion intensity at each material point with the unique reference state of $\beta=0$ when no glide dislocations accumulate inside V. The time rate of change of β in reference to the material frame held fixed with respect to the external observer is now sought. Differentiating equation (5a) with respect to time holding ζ fixed and using equation (4), the following is obtained after rearrangement,

$$\frac{\partial \beta}{\partial t} = \dot{c}\beta - \nabla_{\zeta}\cdot\beta v + b\rho\lambda\partial M + b\rho\lambda\frac{\partial M}{\partial t} + (\lambda\cdot\frac{\partial s}{\partial t})M \qquad (6)$$

where v denotes the glide velocity ($v = v\cdot s$) and spatially independent condition of $\nabla s = \nabla m = 0$ in V were also used. Equation (6) is written in reference to the material frame and in order to express it with respect to the internal observer frame, the internal rotation of dislocations should be considered. To this end it is noted that an accumulation of glide dislocations within a material volume V not only produces internal distortion but also internal rotation. An internal spin tensor ϖ^{I} can then be identified in association with the rotation of slip zones in a fixed material volume. The internal rotation, together with the internal distortion, is believed to be accommodated by the elastic surroundings to compensate the incompatibility due to the accumulation of dislocation. It is emphasized again that here the exclusive concerns are the deformation and rotation process due only to dislocations from an internal observer's point of view. In this way, standard local elastic deformations and rigid body rotations are explicitly excluded.

Next, rate with respect to an internal observer who, by definition, sees no time rate of change of the orientation quantities **s**, **m** and **M** are considered. In view of the spatial

independence assumption for these quantities the co-rotational rates of the vector s and the second order tensor M and β, seen by an internal observer, can then be written as

$$\mathring{s} = \frac{\partial s}{\partial t} - \varpi^{I} \cdot s \,, \qquad (7a)$$

$$\mathring{M} = \frac{\partial M}{\partial t} - \varpi^{I} \cdot M + M \cdot \varpi^{I} \,, \qquad (7b)$$

$$\mathring{\beta} = \frac{\partial \beta}{\partial t} - \varpi^{I} \cdot \beta + \beta \cdot \varpi \,, \qquad (7c)$$

Utilizing these together with the fact that $\mathring{s} = \mathring{M} = 0$, equation (6) can now be reduced into the simpler form of

$$\dot{\beta} + \nabla_{\zeta} \cdot (v\beta) = (\dot{c} + \frac{v}{\lambda})\beta \,, \qquad (8)$$

It is remarked that equation (8) is the evolution equation of β expressed in reference to the material frame and has the form of a complete balance law for tensor variables containing both a flux term and a rate term taken co-rotationally with an "internal observer".

If the material element V is now allowed to move with a velocity **u** in the internal observer frame, the corresponding "plastic spin" W^{P} should be included for the co-rotational rates defined in equations (7a)- (7c). the total dislocation-induced inelastic spin, W^{D} associated exclusively with dislocation motion is then given by

$$W^{D} = \varpi^{I} + W^{P} \qquad (9)$$

3.2. Observable deformation variable

The tensor β is a local variable defined at each material point and thus cannot be measured in principle by an external observer. It is then essential to introduce deformation variables that must be phenomenologically measurable and yet based on which various changes of mechanical behavior can be adequately characterized. A volume average of β as an "internal strain tensor" **a**, is thus defined :

$$\mathbf{a} = \langle\beta\rangle = \frac{1}{V}\int_V \beta \, dV, \qquad (10)$$

where V is an appropriate material volume that must be selected to provide a meaningful measure of the respective local variables. Taking the volume average of each term in equation (8) provides the following kinematic relation

$$\dot{\mathbf{a}} + \frac{\dot{V}}{V}\mathbf{a} + \dot{\boldsymbol{\alpha}} = \dot{\boldsymbol{\varepsilon}} \qquad (11)$$

with the two observable variables $\dot{\boldsymbol{\alpha}}$ and $\dot{\boldsymbol{\varepsilon}}$ defined as

$$\dot{\boldsymbol{\alpha}} = \langle\nabla\cdot(\mathbf{v}\beta)\rangle = \frac{1}{V}\int_S \beta(\boldsymbol{\nu}\cdot\mathbf{n})dA \ , \qquad (12)$$

and

$$\dot{\boldsymbol{\varepsilon}} = \frac{V}{\lambda}\boldsymbol{\beta} = \frac{1}{V}\int_V \rho b \nu \mathbf{M} dV \ , \qquad (13)$$

The unit vector **n** in equation (12) denotes the normal direction to the material boundary S. The sink source term ($\dot{c}\beta$) is neglected in equation (13) by assuming the usual Frank-Read source of glide dislocations [52] located at the center of slip zones.

The tensor variable $\mathring{\mathbf{a}}$ defined as the volume average of the symmetric part of the internal distortion in equation (10) provides an effective measure of the internal distortion due to the stored dislocations within the time. The rate variable $\dot{\alpha}$ involving the surface integral in equation (12) is referred to as the "plastic strain rate tensor" since it is caused by

the outward flux of dislocations across the material boundary S representing the irreversible and non-recoverable rate process of relieving the internal strain". This brings up the possibility of utilizing such an internal-variables description to unify various "externally observable physical phenomena" such as plasticity, creep, crack propagation and phase transformations among others. The remaining integral defined in equation (13) is referred to as the "inelastic strain rate tensor" representing the total rate of inelastic deformation, similar to that of Orowan's relation for the mobile dislocation induced strain rate

3.3. Constitutive relations

It can be easily seen from equation (10), (11) and (13) that a mechanic description of **a**, $\dot{\boldsymbol{\alpha}}$ and $\dot{\varepsilon}$ can be accomplished when the relationships of density ρ and flux $\boldsymbol{j} = \rho \mathbf{v}$ to appropriate loading parameters are known. For this purpose, a double-ended pile-up model of straight edge dislocations is considered. For this simple model, equation (10) now takes the form of

$$a = b\eta l^2 M \int_{-1}^{1} y\rho(y)\, dy = 2\, a\, M \qquad (14)$$

With $y = (\lambda / l)$ and η denoting the slip zone density. The density function $\rho(y)$ must be determined by including the effect of dislocation generation and flux across the barriers. $\rho(y)$ in a general form of $\rho(y) = \sigma^I \emptyset(y)/Gb$ is prescribed with G denoting shear modulus and $\boldsymbol{\sigma}^I = \sigma^I M$ responsible for driving dislocations against the long-range interaction forces due to the pile-up dislocations. The remaining part of stress $\sigma^F = 2\sigma^F M$ is used for driving dislocations against the lattice friction force so that the applied stress may be decomposed into an internal stress σ^I and a friction stress σ^F as follows ;

$$\boldsymbol{\sigma} = \boldsymbol{\sigma}^I + \boldsymbol{\sigma}^F \qquad (15)$$

In view of the above relationship, the following three dimensional constitutive equation, similar to that of Hart, are easily arrived at ;

$$a = S:\sigma^I \qquad (16)$$

with the extra dividend that the fourth-order tensor **S** is now explicitly given by the relationship,

$$\mathbf{S} = \frac{\eta l^2}{G}\int_{-l}^{l} y\emptyset(y)dy MM. \qquad (17)$$

A similar expression can be found for the plastic strain rate tensor. In fact, for a double-ended pile up with the length $2l$, equation (12) reduces to

$$\dot{\alpha} = 2b\eta l j^B M = 2\dot{\alpha} M \qquad (18)$$

with j^B denoting the dislocation flux at the barrier. It then follows that

$$\dot{\boldsymbol{\alpha}} = \frac{\dot{\alpha}}{2\sigma^I}\sigma^I = \frac{\dot{\alpha}}{a} S:\sigma^I \qquad (19)$$

providing again a three-dimensional constitutive relationship for $\dot{\alpha}$. To proceed further an expression for j^B is needed which should depend on the temperature, barrier structure, the mechanical driving force, f^B , and resistance forces, f^*, respectively. In view of the physical conditions that $j^B = 0$ for $f^B = 0$ and $j^B \to \infty$ as $f^B \to f^*$ for an activation type of kinetics process, the following is proposed:

$$(f^B / f^*) = \exp[-(j_0^B / j^B)^p] \qquad (20)$$

where j_0^B is a reference flux when $(f^* / f^B) = e$ and the exponent p characterizes dislocation permeability through barriers and thus depends on the barrier properties including its geometry. For the case of plastic distortion, the Peach-Koehler type forces may be used to replace (f^B/f^*) by (σ^I/σ^*) and the flux term (j_0^B / j^B) also can be replaced by $(\dot{\alpha}^*/\dot{\alpha})$ to yield

$$(\sigma^*/\sigma^I) = \exp(\dot{\alpha}^*/\dot{\alpha})^p . \qquad (21)$$

Equation (21) is identical to the "plastic equation of state" proposed by Hart [53] except that the permeability parameter, p, replaces the phenomenological parameter, λ. To account for the temperature effect, it is noted that the reference rate $\dot{\alpha}^*$ is related to j_0^B to prescribe the following relationship also similar to that of Hart;

$$\dot{\alpha}^* = \nu^I(\sigma^*/G)^{n^I} \exp(-Q^I/RT) \qquad (22)$$

with ν^I and Q^I denoting the jump frequency and the activation energy of leading dislocation at the barrier. In equation (22), R is the gas constant and n^I is a material constant.

Finally, the total inelastic strain rate given in equation (13) can now be expressed as

$$\dot{\varepsilon} = b\eta l \int_{-1}^{1} j(y)\, dy MM \cong b\eta l\, j^L\, M = 2\dot{\varepsilon}M \qquad (23)$$

with j^L now denoting an average value of dislocation flux within a slip zone. Since the dislocation glide within a slip zone is governed by the lattice friction force related to ρ^F, equation (23) can be written in a tensorial form ;

$$\dot{\boldsymbol{\varepsilon}} = \frac{\dot{\varepsilon}}{\sigma^F}\boldsymbol{\sigma}^F \qquad (24)$$

The flux j^L should, in general, depend on the temperature, lattice structure and the driving force $(f_L - f_0)$. This flux must satisfy the physical conditions signifying a viscous drag process with $j^L = 0$ for $f_L \le f_0$ and $j^L \to \infty$ as $(f_L - f_0) \to \infty^*$ where f_L is the force required for dislocations to overcome the short-range resistance forces including the threshold friction force f_0. The following power law relationship can then be proposed;

$$(j^L / j_0) = [(f_L - f_0)/f_0]^{1/M} \qquad (25)$$

where M is constant and j_0 is a reference flux when $f_L = 2f_0$.

Replacing the flux ration by the strain rate ration $(\dot{\varepsilon}/\dot{\varepsilon}_o)$, from the relationship given in

equation (23), equation (24) reduces to the usual power law relationship between $\dot{\varepsilon}$ and σ^F ;

$$(\dot{\varepsilon}/\dot{\varepsilon}_o) = [(\sigma^F - \Sigma_o)\,\Sigma_o]^{1/M} \qquad (26)$$

with Σ_o denoting a static lattice friction stress. The temperature effect can be accounted for through j_0 which is in turn related to $\dot{\varepsilon}_o$,

$$\dot{\varepsilon}_o = \nu^F(\Sigma_o/G)^{n^F} \exp(-Q^F/RT) \qquad (27)$$

with ν^F and Q^F denoting the jump frequency and the activation energy of glide dislocation to overcome the lattice friction.

3.4. Constitutive relationship for High temperature deformation

Generally, applied stress decomposes into an internal stress σ^I responsible for driving dislocations against the long-range interaction forces due to the pile-up dislocations and lattice friction force σ^F used for driving dislocations against friction glide resistance between dislocation and lattice as follows;

$$\sigma = \sigma^I + \sigma^F \qquad (15)$$

The constitutive relation for plastic strain rate $\dot{\alpha}$ can be formulated as a kinetic equation of the mechanical activation process of leading-dislocation by internal stress. For uniaxial tension, the scalar relation is expressed in a similar form to that of Hart as

$$(\sigma_\alpha^*/\sigma^I) = \exp(\dot{\alpha}^*/\dot{\alpha})^p . \qquad (28)$$

and

$$\dot{\alpha}^* = \nu^I(\sigma_\alpha^*/G)^{n^I} \exp(-Q_\alpha^I/RT) \qquad (29)$$

Since a grain boundary is an atomic-level interface with low cohesive force and high diffusivity compared to a grain matrix, GBS can be regarded as a stress-induced viscous flow under a frictional drag and we have the following scalar relation between the applied

stress and GBS rate ;

$$(\dot{g}/\dot{g}_o) = [(\sigma - \Sigma_g)/\Sigma_g]^{1/M_g} \qquad (30)$$

and

$$\dot{g}_o = \nu^g(\Sigma_g/\mu^g)^{n^g} \exp(-Q^g/RT) \qquad (31)$$

As like plastic strain rate $\dot{\alpha}$, Dislocation creep strain rate $\dot{\beta}$ can be formulated also as a kinetic equation of the mechanical activation process of leading-dislocation by internal stress.

$$(\sigma_\beta^*/\sigma^I) = \exp(\dot{\beta}^*/\dot{\beta})^p . \qquad (32)$$

and

$$\dot{\beta}^* = \nu^I(\sigma_\beta^*/G)^{n^I} \exp(-Q_\beta^I/RT) \qquad (33)$$

With this additional strain rates, the total inelastic strain rate $\dot{\varepsilon}_T$ must now be written by adding $\dot{g}$ and $\dot{\beta}$ to equation (11) as

$$\dot{\varepsilon}_T = \dot{a} + \dot{\alpha} + \dot{\beta} + \dot{g} \qquad (34)$$

neglecting the volume change rate neglecting the volume change rate *V*. From this kinematic relationship together with the stress relationship given by equation (15), a rheological model for high temperature deformation can naturally be constructed as shown in Fig.10. together with a physical model [54]. In this model, GMD means the grain matrix plastic deformation accommodating incompatibilities due to stress-induced viscous drag.

At high homologous temperature of $T>0.5T_M$ the friction stress $\boldsymbol{\sigma}^F$ is very small compared to the internal stress $\boldsymbol{\sigma}^I$ to give $\sigma \cong \boldsymbol{\sigma}^I$, where T_M is the melting temperature of material in Kelvin. Also the tests were performed after the flow stress reached a nearly steady state to ensure that $\dot{a} = 0$ ($\mathring{a} = \dot{a}$ under the uni-axial testing condition) to reduce equation (35) into

$$\dot{\varepsilon}_T = \dot{\alpha} + \dot{\beta} + \dot{g} \qquad (35)$$

Under this simplified experimental condition, it is sufficient to know the constitutive relationships of the $\dot{\alpha}$, $\dot{\beta}$ and $\dot{g}$ elements prescribed by equation (28), (32) and (30), respectively.

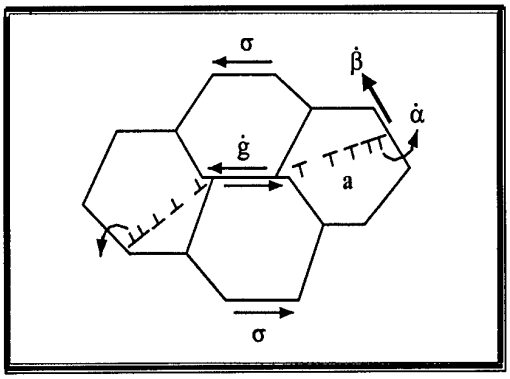

Fig.10. A physical inelastic deformation model for high temperature deformation

4. Experimental procedures

4.1. Specimen preparation

Gamma-TiAl alloy used in this study was supplied by U.E.S, U.S.A. The alloy was skull-melted and isothermally forged at 1260°C with the pressure of 173 MPa for 4 hours. Dimension of the specimen is 50×150×14 mm^3 and the chemical composition of this alloy is shown in Table 2.

Table 2. Chemical composition (at.%) of gamma-TiAl alloy

Al	Cr	Nb	W	B	C	Ti
46.2	1.0	3.0	0.18	0.05	0.12	Balanced

4.2. Heat treatment

With the application of hot working and/or with the variation of heat treatment schedules, four different microstructures can be obtained in the gamma-TiAl alloy. They are; near-γ, duplex ($\alpha_2+\gamma$), nearly lamellar and fully lamellar microstructures. Since duplex microstructure shows the best performance in hot working condition, heat treatment to produce duplex microstructure is adopted in this study.

Specimens were heat treated at 1280°C for 3hr followed by furnace cooling to 800°C and air-cooling to room temperature and final aging treatment at 900°C for 24hr. The resulting microstructure was the duplex microstructure with average grain size of ~12μm. The α_2 -phase grains were observed to form along the gamma grain boundaries and the volume fraction of α_2 -phase is about 5%. In order to vary the α_2 volume fraction,

additional heat treatment was carried out. After heat treating at 1200°C for 3hr followed by air-cooling, the volume fraction of α_2-phase was increased to 30% without changing the average grin size. Mean grain size was measured from the micrographs using linear intercept method and the volume fraction of α_2 and γ phase was measured by the image analysis.

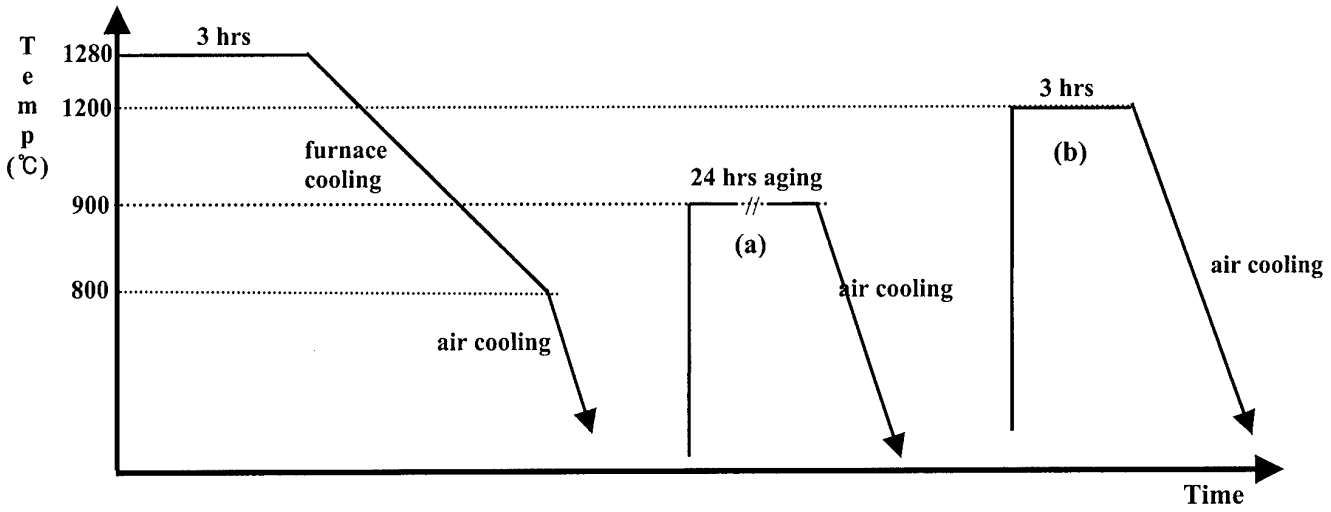

Fig. 11. Schematic diagrams showing the heat-treatments used in this study (a) 5% α_2-phase (b) 30% α_2-phase

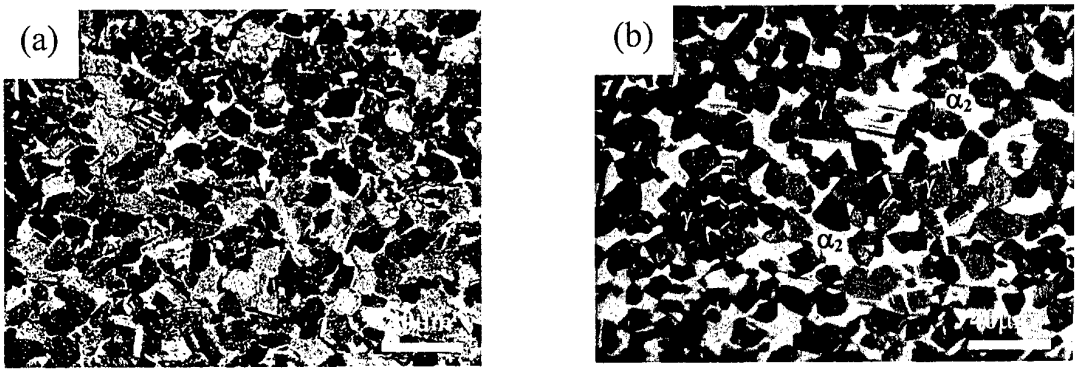

Fig.12. Optical micrographs of heat-treated specimen: (a) 5% α_2-phase volume fraction (b) 30% α_2-phase

4.3. Load relaxation test

A load relaxation test can provide a broad range of strain rates with a minimal plastic strain so that the flow behavior can be obtained without change in internal structure appreciably [55,56].

Load-relaxation tests are carried out using an Instron 1361 testing machine attached to a three-heating-zone furnace capable of maintaining the temperature constant within ±0.5K with respect to both the time and the position along the gauge length. In the load relaxation test, a specimen was deformed first in tension to a certain predetermined strain followed by stopping cross-head motion. The load decrement with time is then monitored and recorded with a digital voltmeter HP 3465A DVM attached to a personal computer for further processing (Fig.13). In order to eliminate systematic fluctuation, the acquired data were filtered by a smoothing module of commercial statistics software under a non-seasonal damping mode. This load-time (P-t) curve (Fig.14) was converted into flow stress vs. inelastic strain rate (σ-$\dot{\varepsilon}$) curve by applying the methods proposed by Lee and Hart [57].

$$\sigma = \frac{P[l_0 + (x - P/K)]}{A_0 l_0} \tag{36}$$

$$\dot{\varepsilon} = -\frac{\dot{P}}{K[l_0 + (x - P/K)]} \tag{37}$$

where, x : displacement of crosshead position

l_0 : initial guage length

A_0 : initial cross section area

K : elastic constant of load train

Because of a high stiffness of hard machine during load relaxation test, it is assumed that the K value during the testing should be constant as follow;

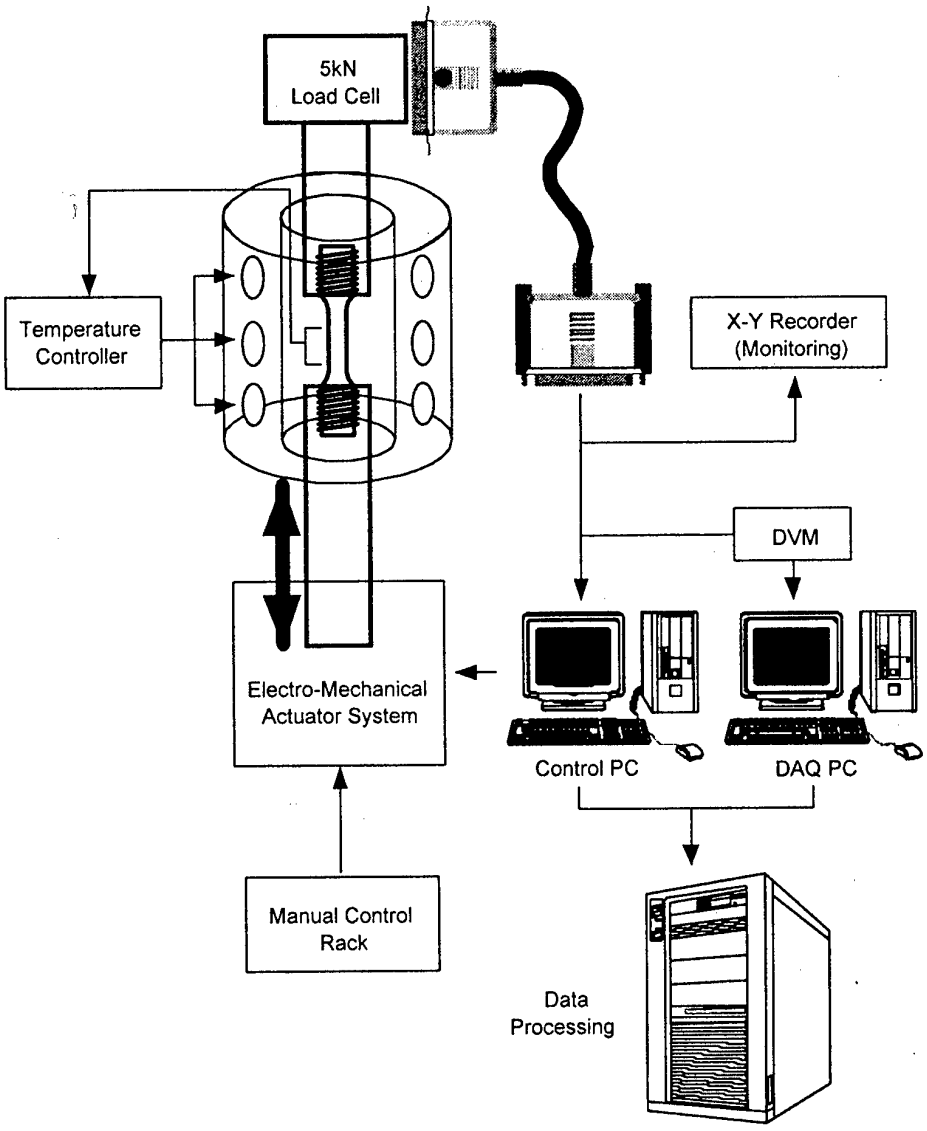

Fig.13. Schematic diagram showing load relaxation test system [63]

$$K = \frac{\dot{p}}{\dot{l}} \qquad (38)$$

In this investigation, load relaxation tests were conducted in Ar atmosphere at temperatures ranging from 800°C to 1020°C. Specimens for the load relaxation tests have gauge dimensions of 27mm in length, 4mm in width and 3mm in thickness (Fig.15.). Microstructures before and after the deformation were analyzed and it was confirmed that microstructures were not largely varied during the load relaxation tests.

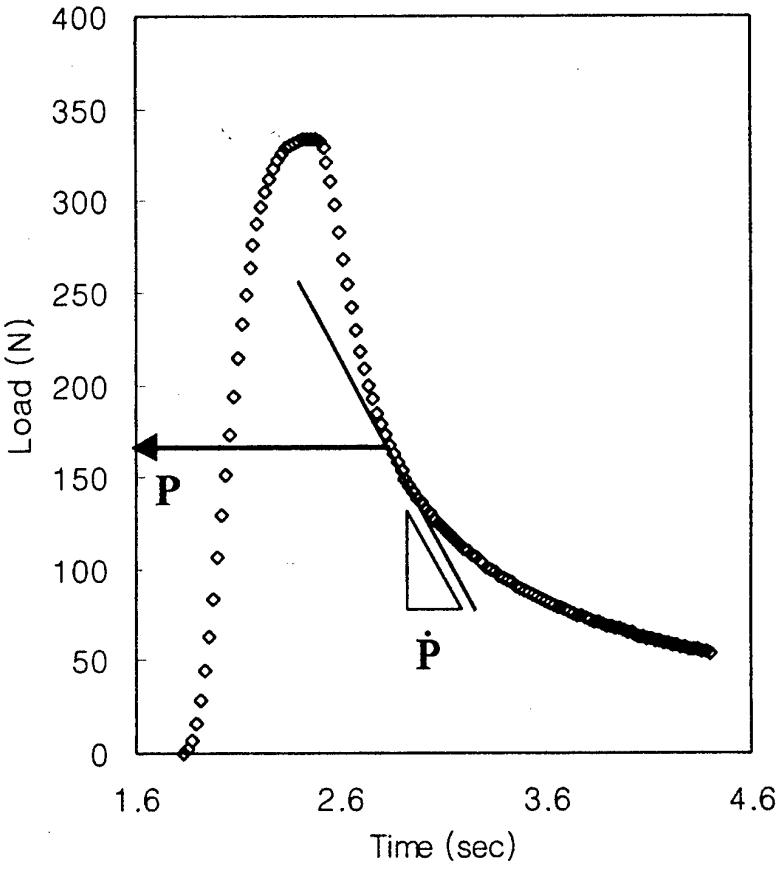

Fig. 14. Typical load-time curve obtained during the load relaxation test

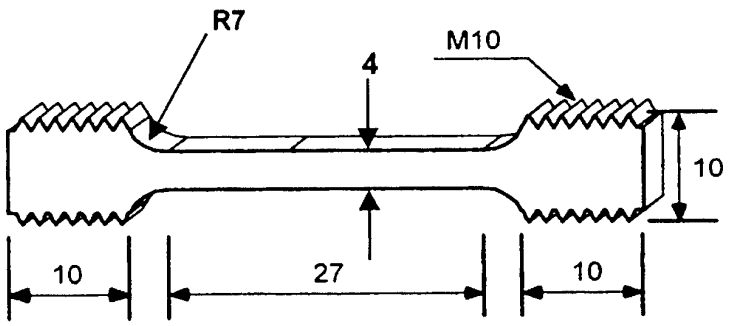

(a) load relaxation test specimen.

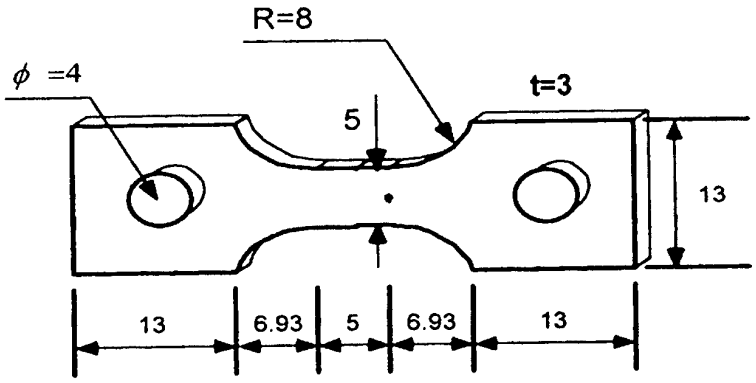

(b) tensile test specimen.

Fig. 15. Specimen for mechanical test

4.4. Tensile test

To determine the effect of amount of deformation and cavity initiation sites, high temperature tensile tests were conducted. Tensile tests were carried out using flat specimens with a gauge dimension of 5mm length, 4mm width and 3mm thickness (Fig.15) on an automated static machine (Instron 1361) equipped with a 5KW halogen lamp furnace (Fig. 16.).

The tests were performed in Ar atmosphere at nominal strain rate ranging from 2×10^{-4}/sec to 5×10^{-3}/sec and temperatures varying from 800°C to 1050°C. After the tensile test, specimens were water-quenched and examined for the microstructural observation.

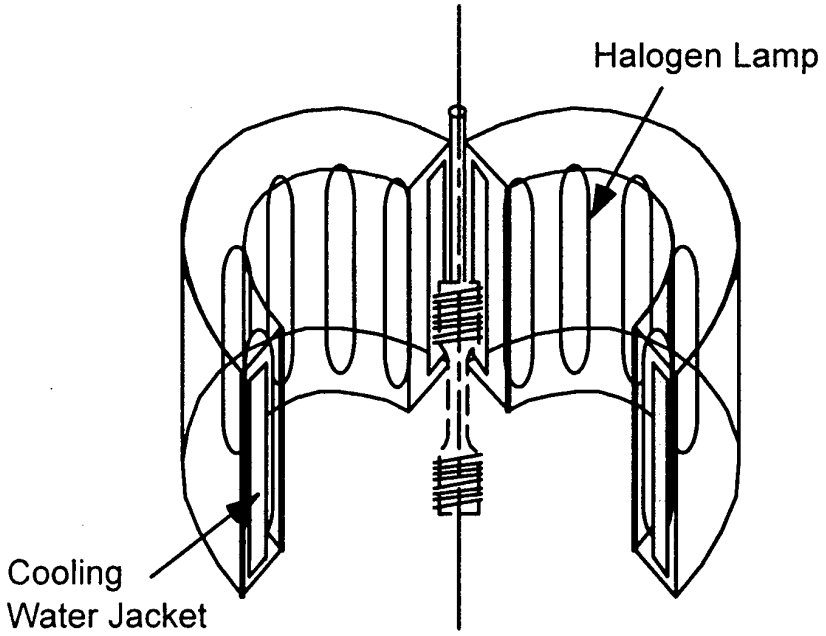

Fig.16. Halogen lamp furnace [63]

4.5. Microstructural observation

Microstructures before and after the deformation were analyzed by optical microscopy. The Kroll's agent (10% HF + 5% HNO_3 + 85% H_2O) was used to etch the specimens.

In order to investigate the cavity initiation sites, the specimens elongated to a tensile stain of 0.5 at 4×10^{-4}/s, 980°C were analyzed by SEM operated in back-scattered-electron mode. Also, the deformed specimens were sliced to a thickness of about 400 μm using an electric discharge machine (EDM) to investigate the internal dislocation structures. Then, thin foils of about 100 μm thickness were prepared by mechanical polishing followed by twin-jet electro-polishing in a solution of 1128ml methanol, 60ml perchloric acid(70%), 72ml nitric acid solution at -18°C under an applied potential of 15V. The thin foil specimens were examined with a transmission electron microscope (TEM).

5. Results

5.1. Flow curves by load relaxation test

The load relaxation test results for the TiAl alloy obtained at temperatures of 800, 880, 980 and 1020°C are shown in Fig.17. It is apparent that the flow curves shift noticeably toward the region of lower stress and higher strain rate as the temperature increases. It is also noticed that flow behavior of 5% and 30% α_2 is different as such that flows stress of 30% α_2 decreases rapidly as lower strain rate ($\dot{\varepsilon} < 10^{-6}$/sec) as compared to that of 5% α_2.

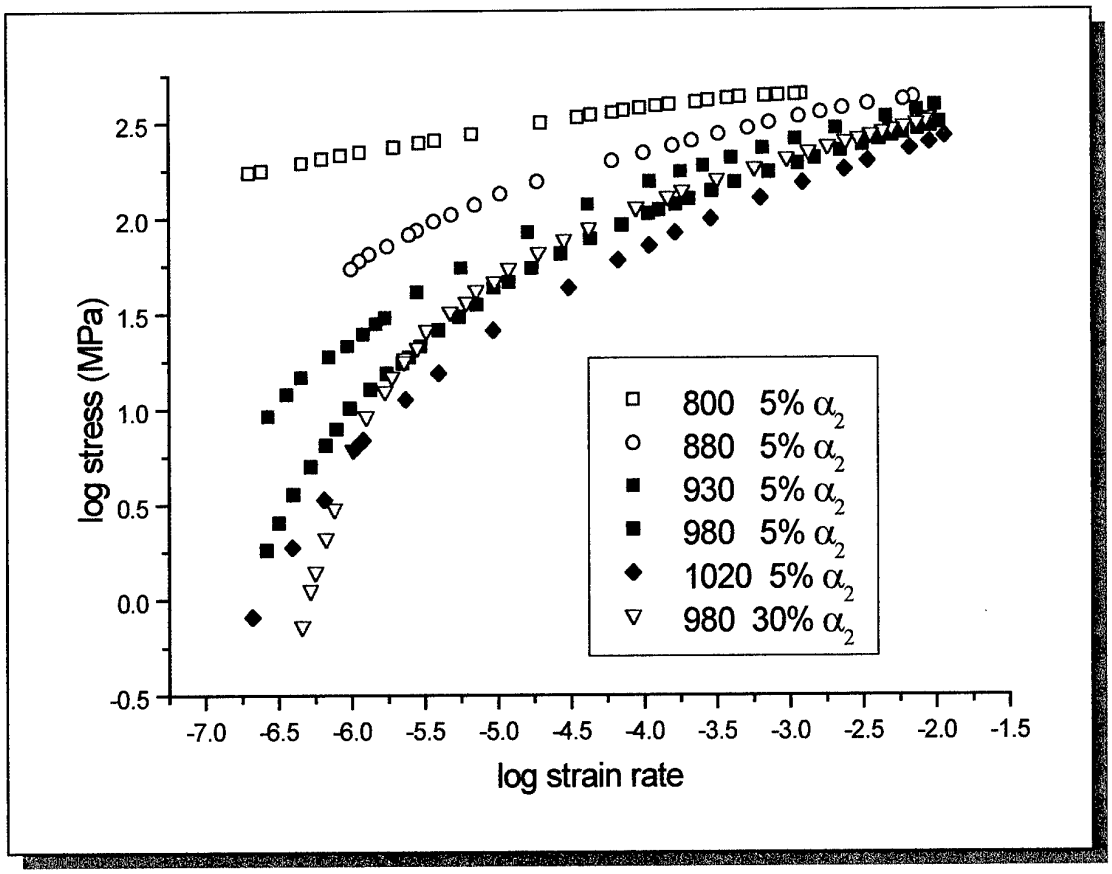

Fig.17. The flow curves of TiAl alloy obtained by load-relaxation tests at various temperatures

To determine the high temperature deformation mechanisms of TiAl alloys at the given small amount of deformation, the flow curve data from load relaxation test have been fitted to the constitutive equation. The data of high stress regions have been first fitted by using equation (28) to trace out the flow behavior of the $\dot{\alpha}$ element and the results are shown in Fig.18 (as red line). The red lines describing the flow behavior of GMD show a good agreement with the experimental data at 800 and 880°C over the entire stain rate region (Fig.18(a), 18(b)). The constitutive parameters (σ_α^*, $\dot{\alpha}^*$ and p) for GMD have been determined from these lines and are represented in Table 3.

The values of $\dot{\beta}$ at low stress level and high temperature are then estimated from the equation (35). Here the grain boundary sliding rate ($\dot{g}$) is assumed to be zero at this temperature range. Then, these values are subsequently used for a non-linear curve fitting of equation (32) to determine the constitutive parameters (σ_β^*, $\dot{\beta}^*$ and p) for dislocation climb. The blue lines in Fig.18 represent the predicted curves for dislocation climb. The curves of dislocation climb are observed only at high temperature and low strain rate region as shown in Fig 18(c), 18(d). The flow curves at various temperatures do not reveal any concave shape, which is an indication of operation of GBS [54,59]. Therefore, it is considered reasonable to assume that $\dot{g}$ equals to zero in this analysis.

The combined curves of GMD and dislocation climb (represented with the green lines in Fig.18(c), 18(d)) have been compared with the experimental data, and a good agreement is observed.

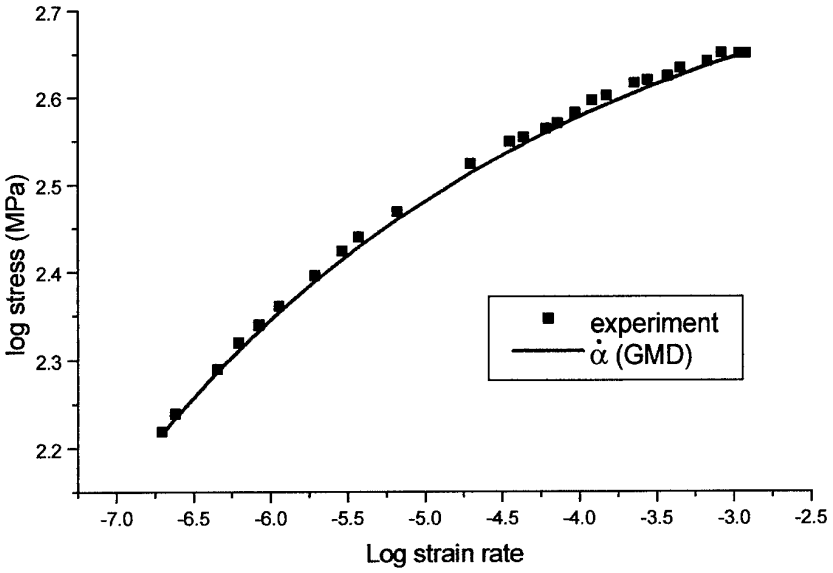

(a) 800 °C

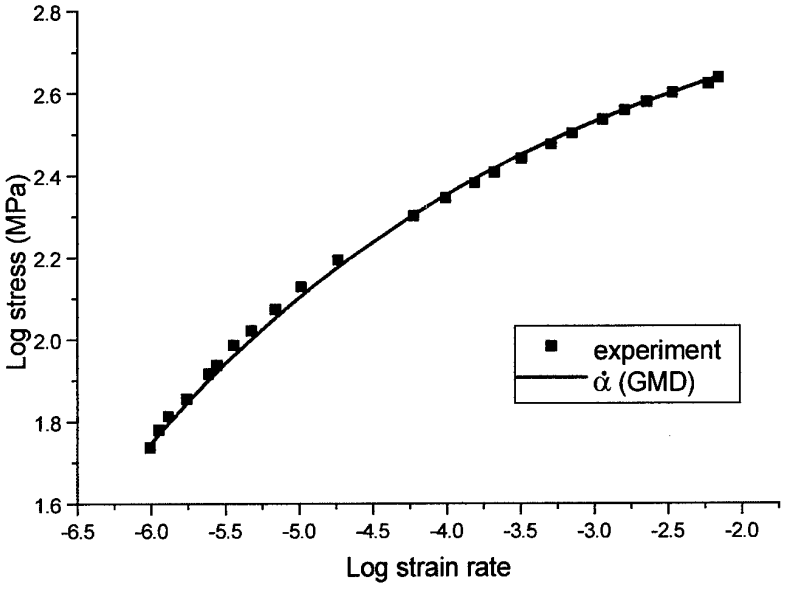

(b) 880 °C

Fig. 18. Continued

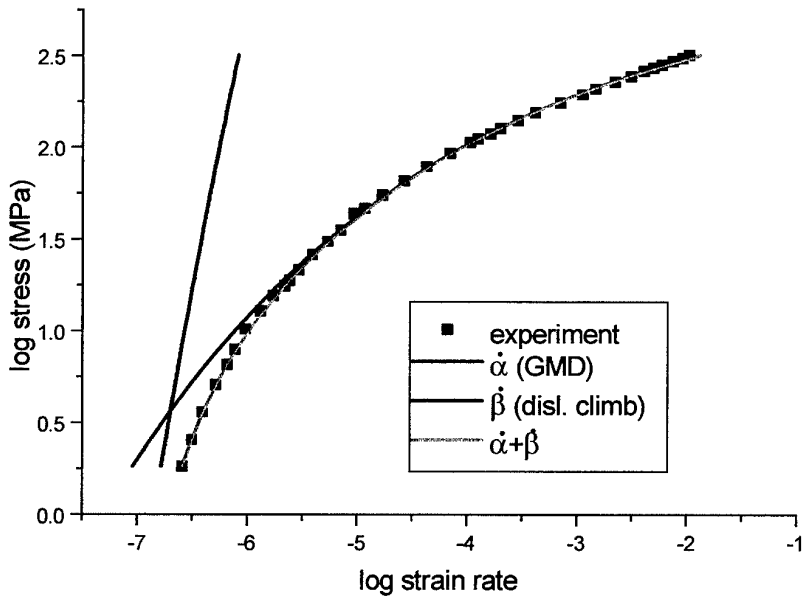

(c) 980 °C

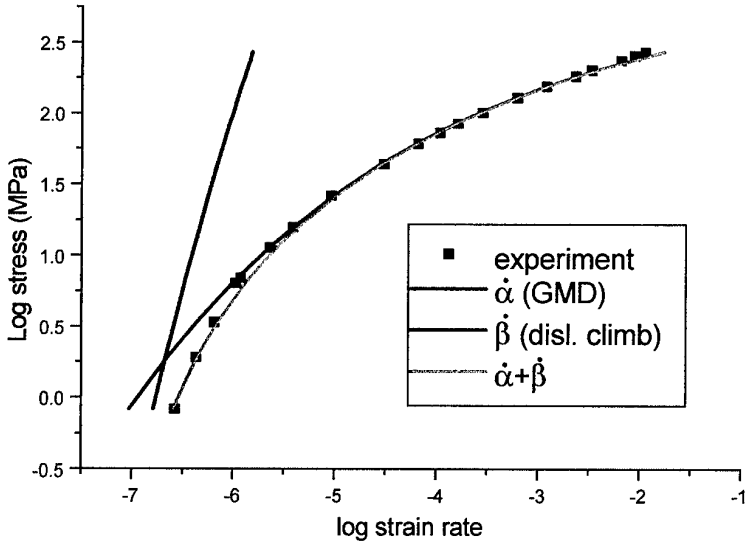

(d) 1020 °C

Fig.18. Predicted flow curves based on the internal variable theory which consists of contributions from grain matrix deformation ($\dot{\alpha}$) and dislocation climb ($\dot{\beta}$). Here the grain boundary sliding rate ($\dot{g}$) is assumed to be zero.

Temp (°C)	GMD			Disl. climb		
	$\log\sigma_\alpha^*$	$\log\dot{\alpha}^*$	p	$\log\sigma_\beta^*$	$\log\dot{\beta}^*$	p
880	2.958	-3.030	0.15			0.15
930	2.971	-2.233		6.864	0.274	
950	2.950	-2.159		6.937	0.920	
980	2.934	-1.822		7.5601	1.251	
1020	2.911	-1.428		7.788	1.451	
980 (30%α_2)	2.957	-1.92568		8.779	2.351	

Table 3. The constitutive parameters determined from load relaxation test at various temperatures

The constitutive parameters for GMD and dis.climb process are presented in Table 3. With the increase in temperature, the reference strain rates of $\dot{\alpha}^*$ and $\dot{\beta}^*$ increases and the internal strength variables $\dot{\sigma}_\alpha^*$ and $\dot{\sigma}_\beta^*$ decrease. The value of parameter p characterizing dislocation permeability of strong barriers is obtained as 0.15 as found in other FCC, BCC structure materials [15,54,59].

Fig.19 and Fig.20 show GMD and dislocation climb creep curves with the variation of temperature, respectively. As the temperature increases, the flow stress in both GMD and dislocation climb creep process decreases. It is apparent that the shape of dislocation climb curves obtained from equation (32) looks like linear one. The mean value of stress exponent n is determined to vary 1.9~ 2.3 at 930°C ~1020°C.

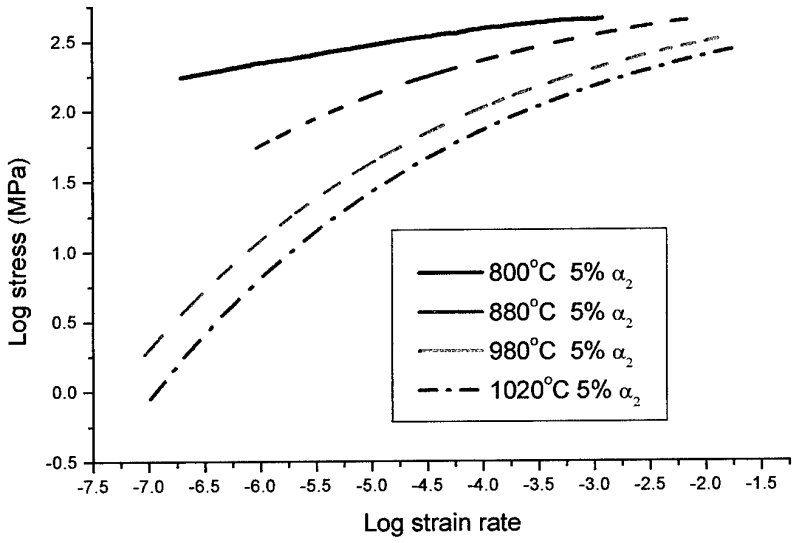

Fig.19. GMD curves at various temperatures

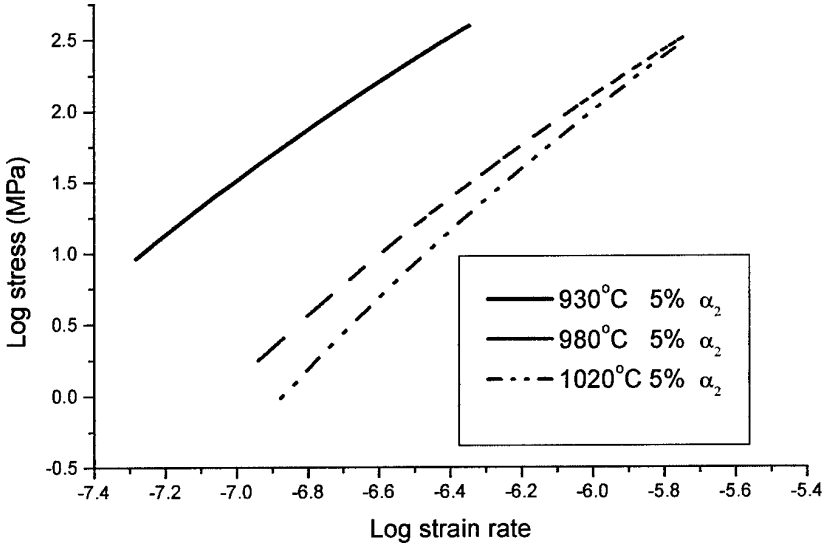

Fig.20. Dislocation climb curves at various temperatures

Therefore, it is concluded that the flow curves of fine-grained TiAl alloy are well described by the combined curves of grain matrix deformation and dislocation climb creep at the given small amount of deformation. It is interesting to investigate the flow behavior when the large amount of deformation is given. Fig.21 shows the result of load relaxation test (at 980°C) for heavily deformed (ε=0.8) specimen. The flow curves are very much different from those of earlier lightly deformed (ε=0.2) specimens since the phenomenon of grain boundary sliding appears (concave upward portion) and prevails the flow behavior. Here the portion of disl.cimb creep is assumed to be zero. Then, the flow behavior is dominated by the GMD and GBS. The experimental data in Fig.21 have been attempted to fit with the combined curve of grain matrix deformation and grain boundary sliding. The green line representing the combined curve shows a good agreement with the experimental data

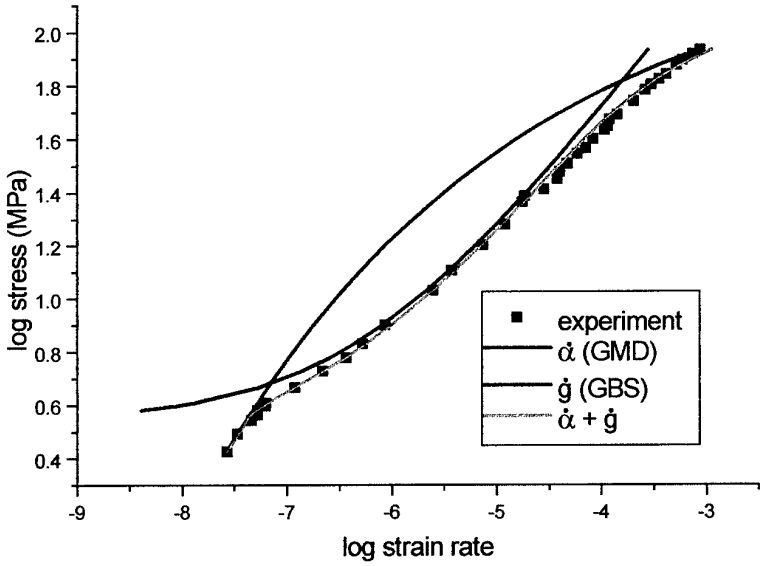

Fig.21. The flow curves of heavily deformed (ε=0.8) specimen at 980°C based on the internal variable theory which consists of contributions from grain matrix deformation ($\dot{\alpha}$) and grain boundary sliding ($\dot{g}$). Here disl.climb creep ($\dot{\beta}$) is assumed to be zero.

5.2 Flow behavior with the variation of α_2/γ phase ratio at 980°C

Fig.22 represents different flow behavior in 5% and 30% α_2 microstructure at 980°C. The flow curves of both microstructures can be also split into GMD and dislocation climb curves. Fig.23 shows the comparison of flow behavior of each deformation mechanism for both 5% and 30% α_2 specimens. As the volume fraction of α_2-phase increases, flow stress of GMD slightly increases and, however, that of dislocation climb creep decreases at a fixed strain rate. The increase in flow stress of GMD is presumably due to the fact that α_2-phase is relatively harder than γ phase and acts as an effective dislocation barrier. As to the reason of lower flow stress for the disl.climb creep at higher α_2 (30% α_2) specimen, it is not clearly understood.

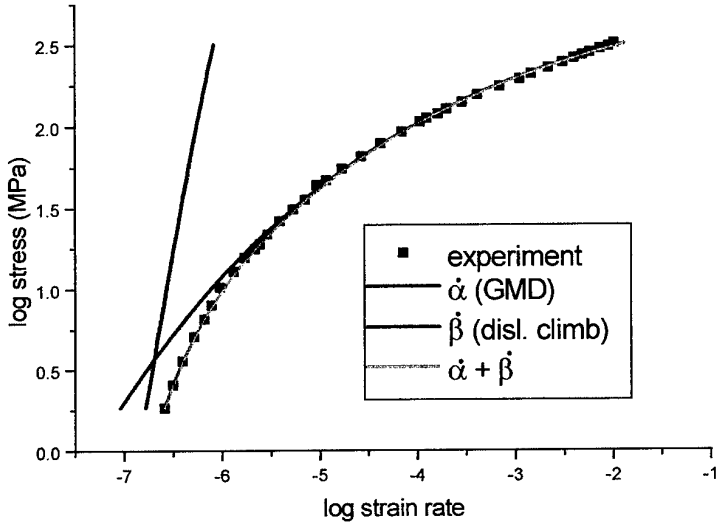

(a)

Fig. 22. Continued

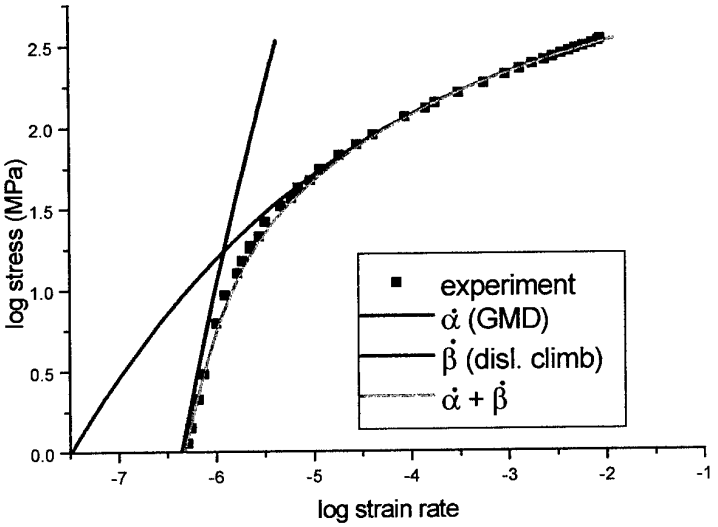

(b)

Fig.22 Flow behavior at 980°C with the variation of α_2/γ phase ratio: (a) 5% α_2 volume fraction (b) 30% α_2 volume fraction

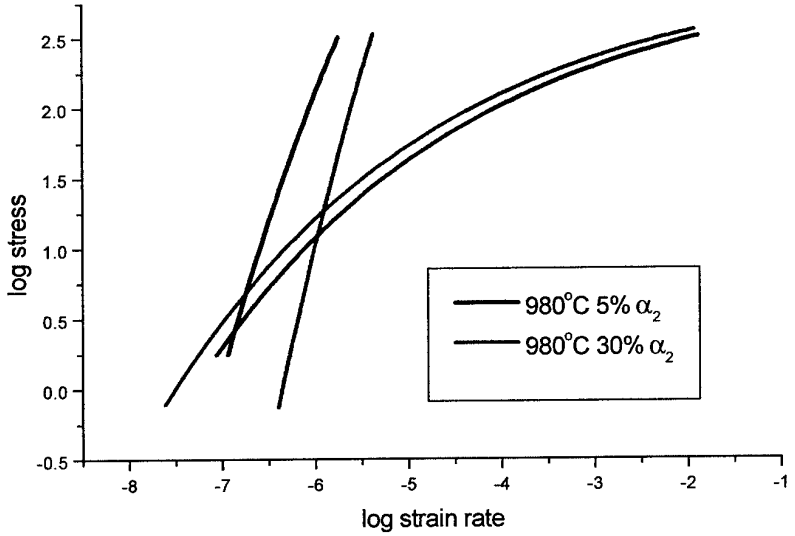

Fig.23 Flow curves for GMD and disl.climb creep at 980°C with the variation of α_2 volume fraction

5.3. High temperature tensile test

The results of tensile tests conducted on γ-TiAl alloy at several initial strain rates and temperatures are given in Fig.24. As the temperature increases and/or strain rate decreases, elongation increases. The largest elongation is obtained at 1050°C and 4×10^{-4}/sec.

Tensile elongation of 30% α_2 is also compared with that of 5% α_2 tested at 980°C and 4×10^{-4}/sec. It is observed that the elongation of 30% α_2 microstructure is smaller than that of 5% α_2 microstructure. Earlier investigations [36,58] on TiAl alloys have shown the benefit of having the large amount of α_2 phase to enhance the mechanical properties. However, our result indicates that there is a lower limit for the α_2 phase, beyond which exist where the ductility leading to a higher tensile elongation, ceases to increase.

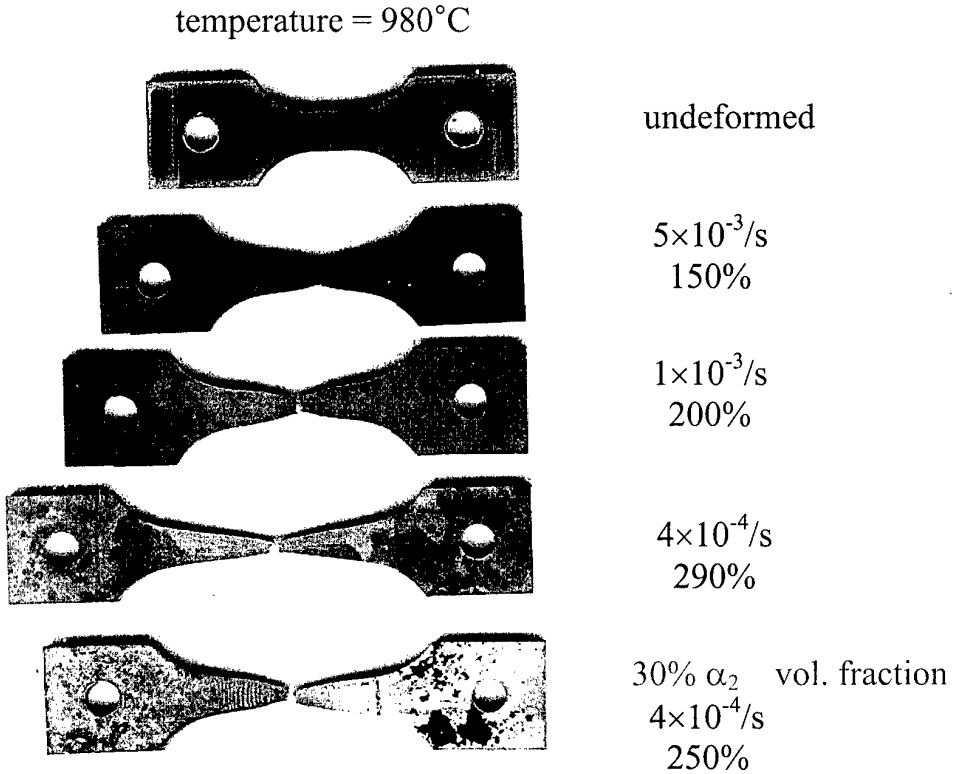

(a)

Fig. 24. Continued

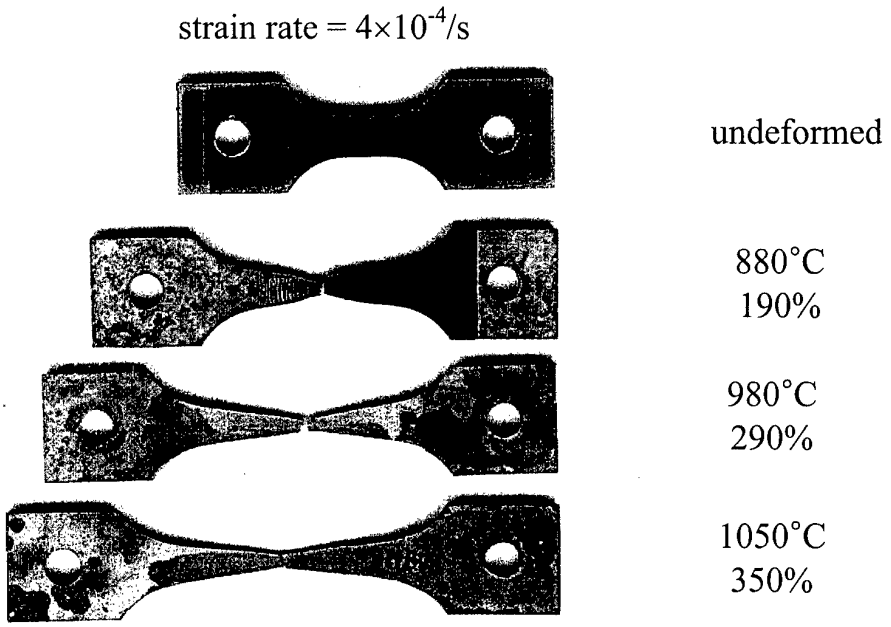

(b)

Fig. 24 Superplastically deformed specimens showing (a) the effects of strain rate and α_2 volume fraction (b) the effect of temperature

5.4. Microstructures after the tensile deformation

The microstructures after the tensile test under various test conditions are analyzed by optical microscopy. Fig.25 shows microstructures observed in longitudinal sections of grip region and the vicinity of fractured area of tensile specimen with a strain rate of 4×10^{-4}/sec at various temperatures. The figures show that the γ grains were refined due to the dynamic recrystallization. The recrystallized grain size increases with increasing the temperatures. The grain shape remains equiaxed and rounded after deformation at 1050 and 980°C. However, γ and α_2 phases are deformed and elongated along the direction to tensile axis at 880°C. Fig.26 shows that the changes in microstructural evolution which occurred with increasing strain

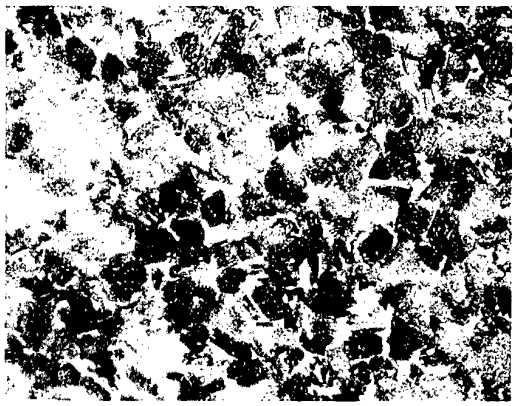

(a) 880°C grip

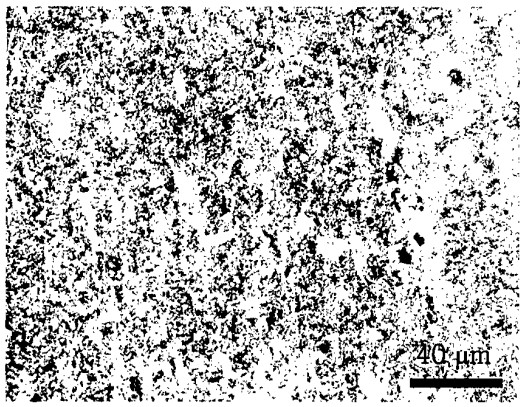

(b) 880°C fracture area

(c) 980°C grip

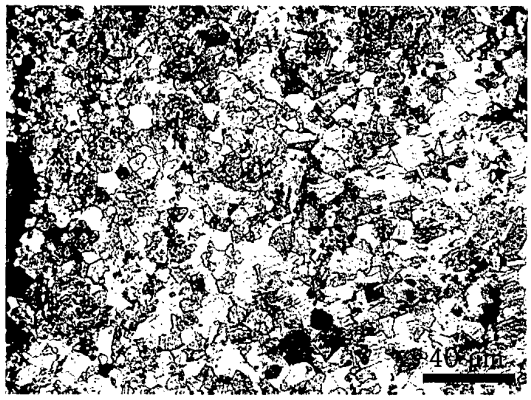

(d) 980°C fracture area

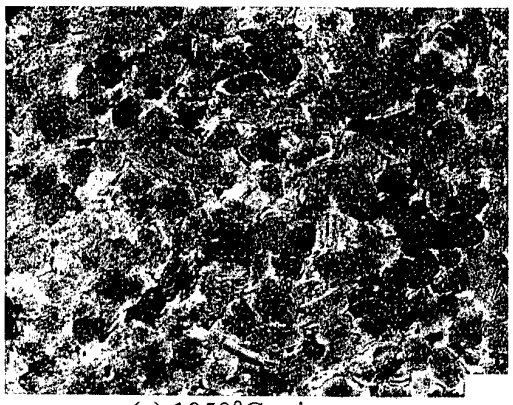

(e) 1050°C grip

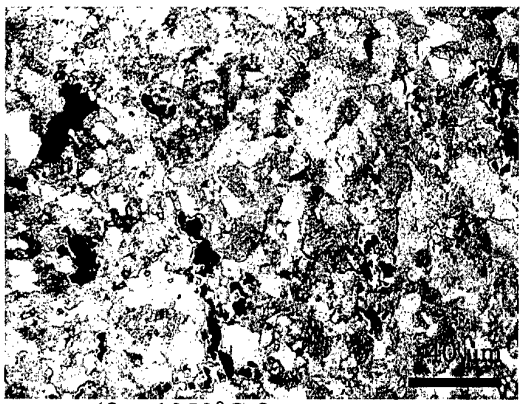

(f) 1050°C fracture area

Fig.25 Optical micrograph showing the effect of temperature on dynamic recrystallization at 4×10^{-4}/s strain rate.

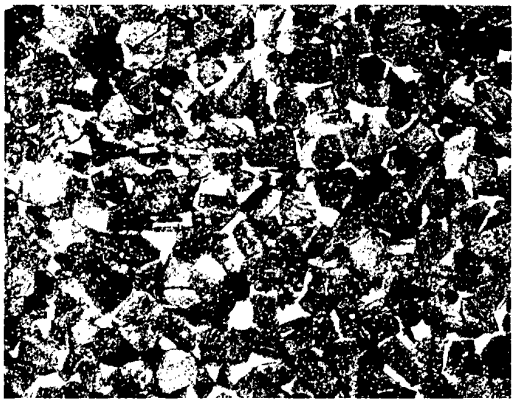

(a) 1×10^{-3} /s grip

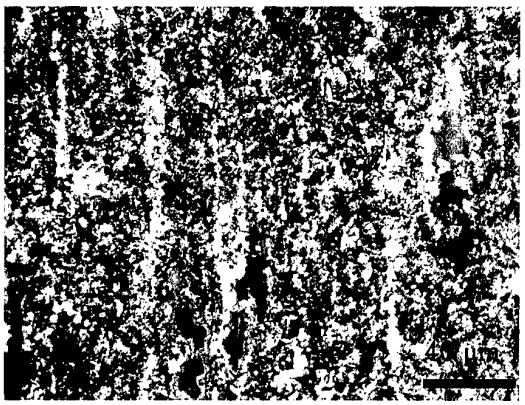

(b)1×10^{-3} /s fracture area

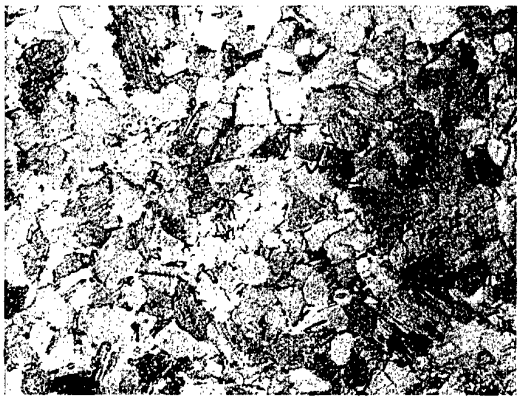

(c) 4×10^{-4} /s grip

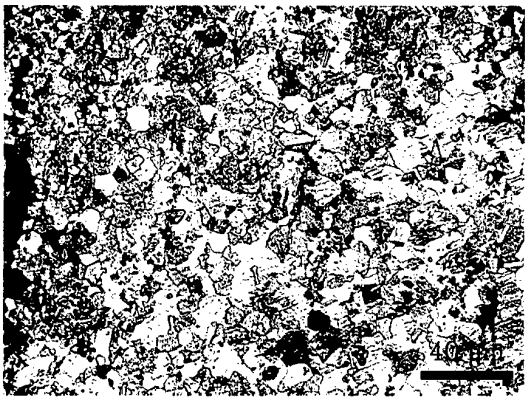

(d)4×10^{-4} /s fracture area

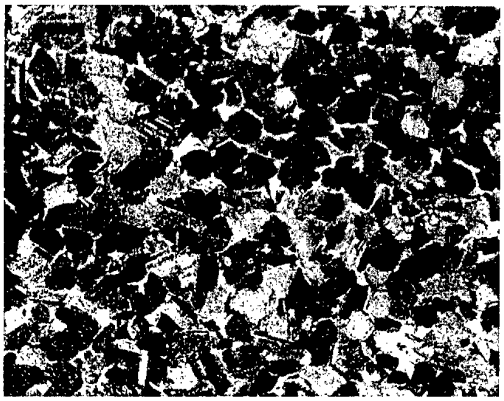

(e) 1×10^{-4} /s grip

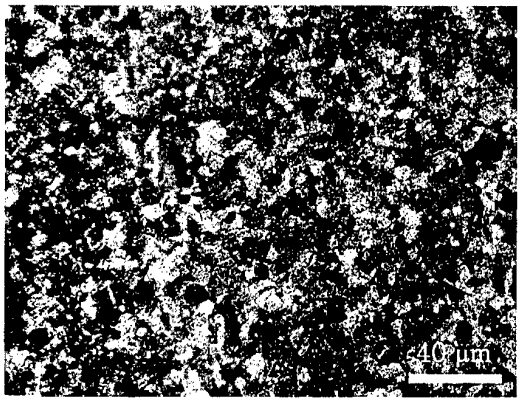

(f)1×10^{-4} /s fracture area

Fig.26 Optical micrograph showing the effect of strain rate on dynamic recrystallization at 980°C.

rate at a fixed temperature of 980°C are similar to those that occurred with decreasing temperature at a fixed strain rate. The recrystallized grain size increases with increasing the temperature and with decreasing the strain rate.

Microstructure of Tensile specimens deformed by a 30% strain at 980°C and 4×10^{-4}/sec are also investigated by TEM. The microstructures of a superplastically deformed specimen are compared to that of an undeformed specimen. As it can be seen in undeformed specimen (Fig.27(a)), few dislocations are observed either inside the grain or along the grain boundary. In the deformed specimen, several types of dislocation structures are observed in the TEM microstructures. One is the structure with high dislocation density in γ phase (Fig.27(b)), which is not recrystallized yet at a given amount of deformation (50% strain). Other microstructure (Fig.27(c)) shows the grain with a very low dislocation density indicating that this grain is a recrystallized one. In addition, microstructure with higher dislocation density in γ grains than in α_2 grains is observed (Fig.27(d)). The shape of α_2-grain boundary remains unchanged as sharp and straight boundary.

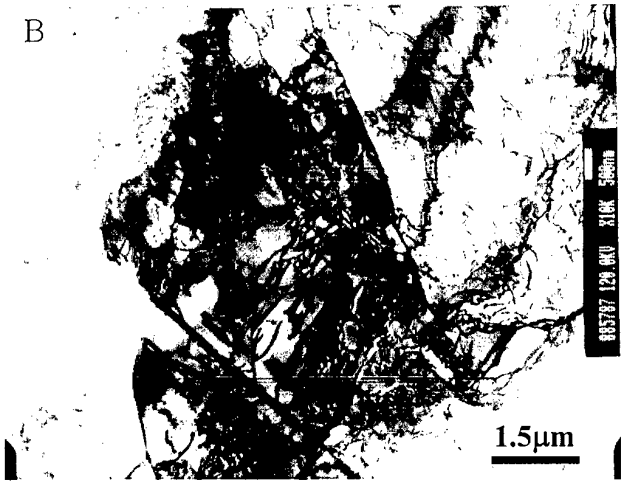

Fig. 28. Continued

Fig. 28. T.E.M. micrograph showing dislocation structure

5.5. Cavity initiation site observation

To determine the cavity initiation sites, tensile specimens deformed by a 100% strain in tension at 980°C and strain rate of 4×10^{-4}/sec are investigated. Since the observations at other test conditions were similar, only those for intermediate temperature and strain rate are presented here.

Which there have been few cavities at the region far from the fracture area that had experienced a low strain, the region near the fracture area has revealed relatively high density of cavities. Thos cavities have been taken on SEM-Back scattered electron image as shown in Fig. 28. The darker phase and α_2-phase is identified as γ-phase and the lighter phase is determined as α_2-phase. It is clearly seen in Fig.28 that most of cavities initiate at α_2/γ boundaries as well as at γ/γ boundaries and the average size of cavities is less than 1μm.

The number of cavities produced in α_2/γ, γ/γ and α_2/α_2 boundaries were quantitatively measured on the fracture area, and the results are listed in Table.4

	γ/γ	α_2/γ	α_2/α_2
Actual numbers of cavities	55	22	
Normalized numbers of cavities	58	430	

Table.4 Measured and normalized number of cavities

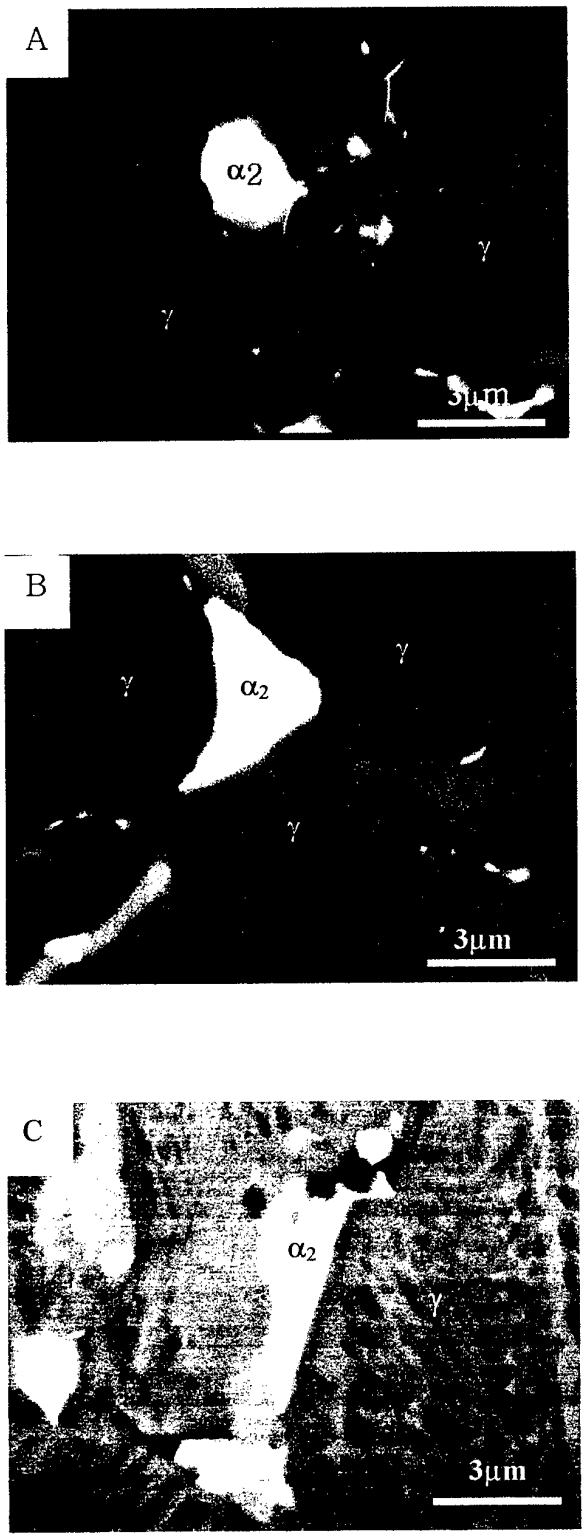

Fig.28. Back scattered electron micrograph showing cavity initiation site

Actually, a larger number of cavities are observed at γ/γ boundaries than α_2/γ boundaries. However, the normalized number of cavities shows which has been calculated by dividing actual number of cavities with phase volume fractions of constituent phases shows reverse trend. Cavities at α_2/α_2 boundary are scarcely observed due to small volume fraction of α_2 phase in this specimen.

6. Discussion

6.1. Deformation mechanisms from inelastic deformation theory

It is worthwhile to discuss here how the deformation mechanisms such as grain boundary sliding, dynamic recrystallization, dislocation climb and grain matrix deformation contribute to the total deformation of fine-grained TiAl alloy at high temperature, since each mechanism plays an important role, respectively, in high temperature deformation of TiAl alloy.

Fig.29 schematically shows the changes in dominant deformation mechanisms at the stage of small, intermediate and large deformation, respectively. In the early stage of the deformation, flow behavior is mainly governed by grain matrix deformation and dislocation climb. The evidence of grain boundary sliding was not observed in the optical micrographs as well as load-relaxation tests. Dislocation climb process is frequently accompanied by grain matrix deformation since many pile-up dislocation at grain boundary resulted from the grain matrix deformation can climb easily at high temperature, thereby relieving the stress concentration. It is interesting to observe that the contribution of grain boundary sliding to the overall deformation is negligible at the early stage of deformation in the temperature range of 800~1050°C.

On the other hand, at the intermediate strain of about 30% elongation, dynamic recrystallization starts to occur, which effectively prevents neck formation during the deformation. Moreover, the grain size becomes finer due to formation of dislocation- free new grain. At the large deformation, flow curves of TiAl alloy are split into grain matrix deformation and grain boundary sliding while dislocation climb process does not seem to play any significant role at this stage during the large deformation. Grain boundary sliding is more viable with microstructural change and contributes noticeably to total deformation

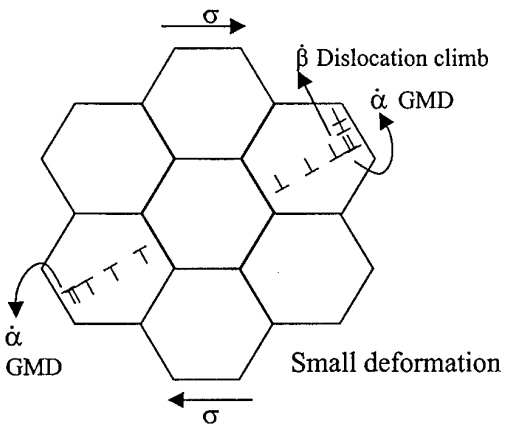

(a)

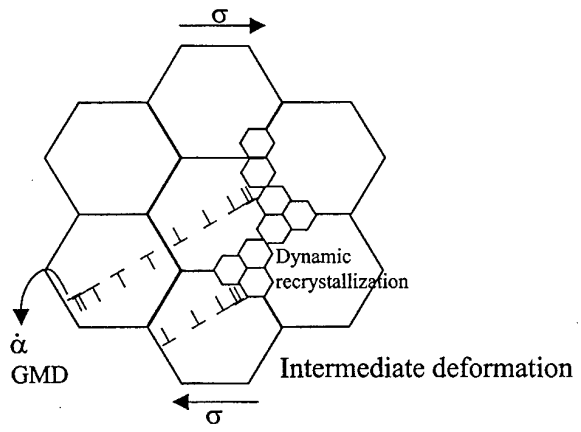

(b)

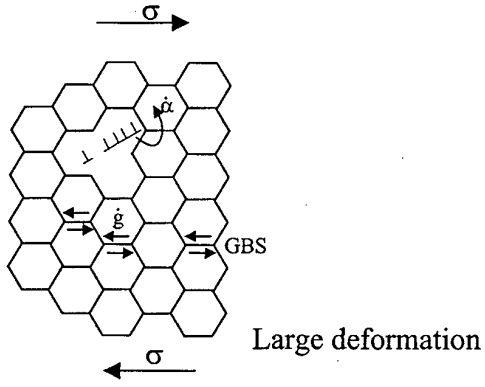

(c)

Fig.29. Schematic illustration showing the change of deformation mechanism with the increase of deformation.

of TiAl. That is to say, grain boundary sliding is enhanced by grain refinement due to dynamic recrystallization.

Fig.30 clearly shows dynamic recrystallization behavior as strain increases. The fraction of recrystallized grains increases with the increase of the imposed strain. It appears in Fig.30 that dynamic recrystallization continuously take place even after grain boundary sliding occurs. For the coarse grained microstructure, grain boundary sliding is difficult to occur. Therefore local stress concentration is easily developed at the grain boundary due to the dislocation pile-up. However, the accumulation of dislocations favorably induces dynamic recrystallization resulting in grain refinement, which in turn makes grain boundary sliding phenomena become more operative.

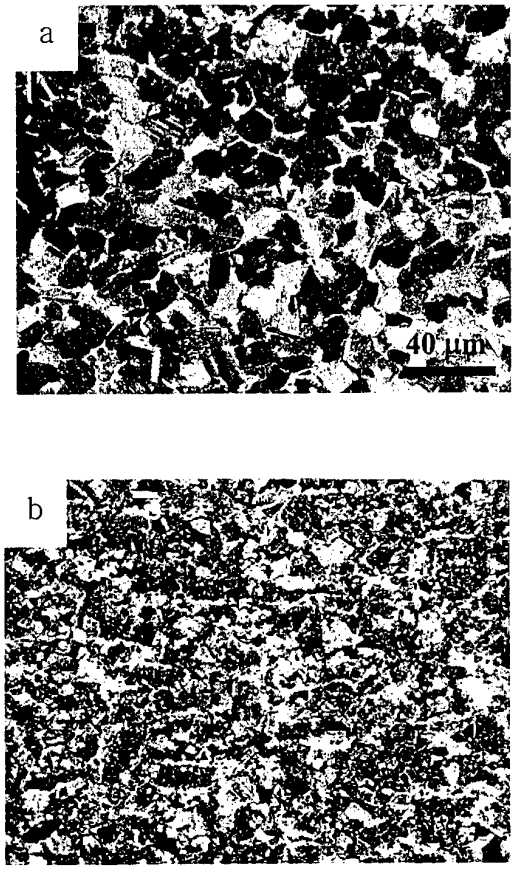

Fig.30 Continued

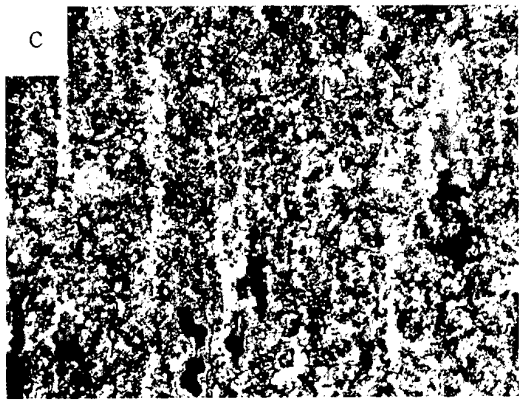

Fig.30 Optical micrographs showing microstructural change due to dynamic recrystallization at 980°C. ; (a) undeformed (b) ε = 0.8 (c) ε =2.0

The recrystallized grain size is not only important for superplastic deformation but also sensitive to deformation temperature and strain rate. It has been observed that the recrystallized grain size increases with either increasing temperature or decreasing the strain rate, i.e. with decreasing the Zener-Hollomon parameter. Grain size continuously decreases due to dynamic recrystallization from initial large grain to smaller grains. As a result, grain boundary sliding becomes a dominant mechanism while dynamic recrystallization and grain refinement cease to occur. Since the grain size for grain boundary sliding at high Zener-Hollomon parameter region is relatively smaller than at low Zener-Hollomon parameter region, the recrystallized grain size must be small at high Zener-Hollomon parameter region. The variation of recrystallized grain size with the Zener-Hollomon parameter is plotted in Fig.31.The dependence of recrystallized grain size on Zener-Hollomon parameter has been formulated as Equation (36):

$$D_{rex} = (2.00\times10^5)\cdot Z^{-0.490} \qquad (36)$$

where D_{rex} is the recrystallized grain size, Z is the Zener-Hollomon parameter

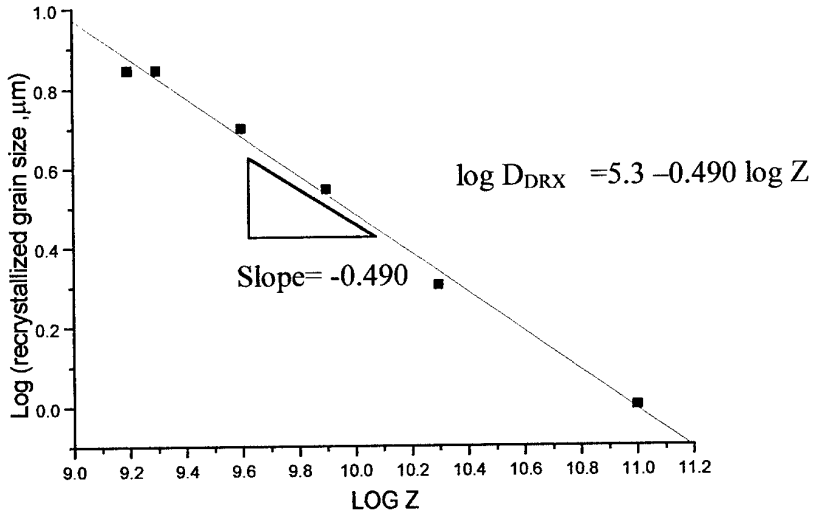

Fig.31 The variation of recrystallized grain size with the Zener-Hollomon parameter

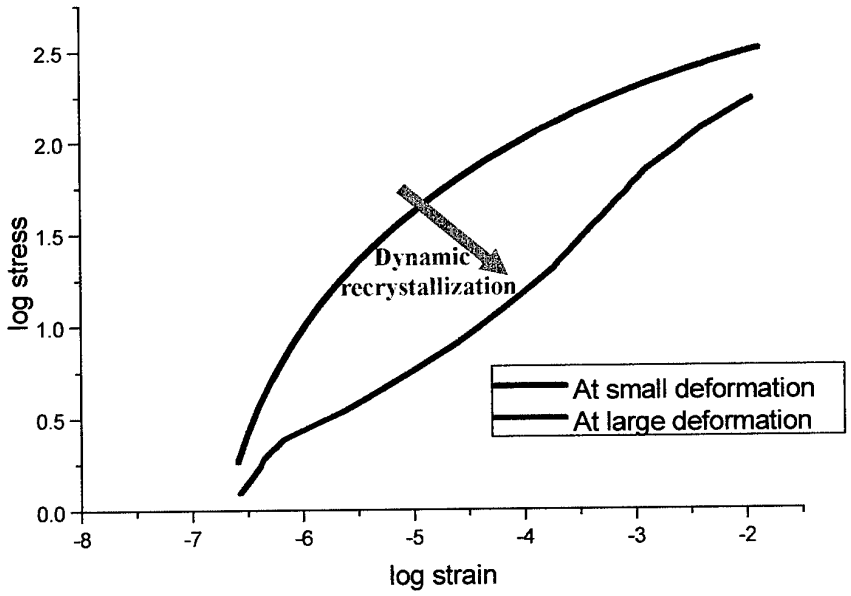

Fig.32 Schematic diagram showing change of deformation mechanism due to dynamic recrystallization at large deformation.

6.2. Constitutive parameters analysis

The constitutive parameters listed in Table 3 can adequately describe the effect of temperature on flow curve of TiAl alloy. Both the reference strain rates $\dot{\alpha}^*$ and $\dot{\beta}^*$ increase with increasing temperature, which is relevant to the shift of flow curve (to the region of higher strain rate and lower stress). It has been noted that σ_β^* increases as the temperature increases, while σ_α^* remains relatively insensitive to the test temperatures in this study. The value of parameter p characterizing dislocation permeability of strong barriers, i.e grain boundaries, has been obtained as 0.15 regardless of test temperatures, which also agrees with those reported in other FCC, BCC and HCP structural materials [59,60].

In order to describe the flow behavior, the parameters given in equation (29) and (33) have to be determined in the following ways. Since the internal strength (σ_α^*) is almost constant within the temperature range used in this study, a differential relation of equation (29) is obtained in the form of

$$\left.\frac{\delta \ln \dot{\alpha}^*}{\delta (1/\mathrm{T})}\right|_{\sigma^*} = -\left(\frac{Q^I{}_{GMD}}{R}\right) \qquad (37)$$

The activation energy (Q^I) for the GMD process can be calculated by a linear regression method as depicted in Fig.33. From the analysis of experimental data, the value of Q_{GMD} has been found to be approximately 319kJ/mol. The activation energy for self-diffusion of Ti and Al is roughly 260kJ/mol and 370kJ/mol, respectively. It is obvious that the value of Q_{GMD} = 319kJ/mol calculated from this study is somewhat equal to the average value of self-diffusion energy of Ti and Al [61], which implies that movement of dislocation are largely affected by the diffusion of Ti and Al.

It is more difficult to determine the activation energy for dislocation climb because of

the differential relation between σ_β^* and temperature as shown in equation (37). In this study, the experimental data were fitted by the multiple regression method using equation (33) directly. The activation energy of $Q_{disl.\ climb}$ has been found to be 386 kJ/mol, which seems to support the phenomenological fact that activation energy of dislocation climb is generally higher than that of grain matrix deformation. However, The activation energy for dislocation climb is somewhat lower than that of a previous study [62] in which the influence of grain matrix deformation has been considered.

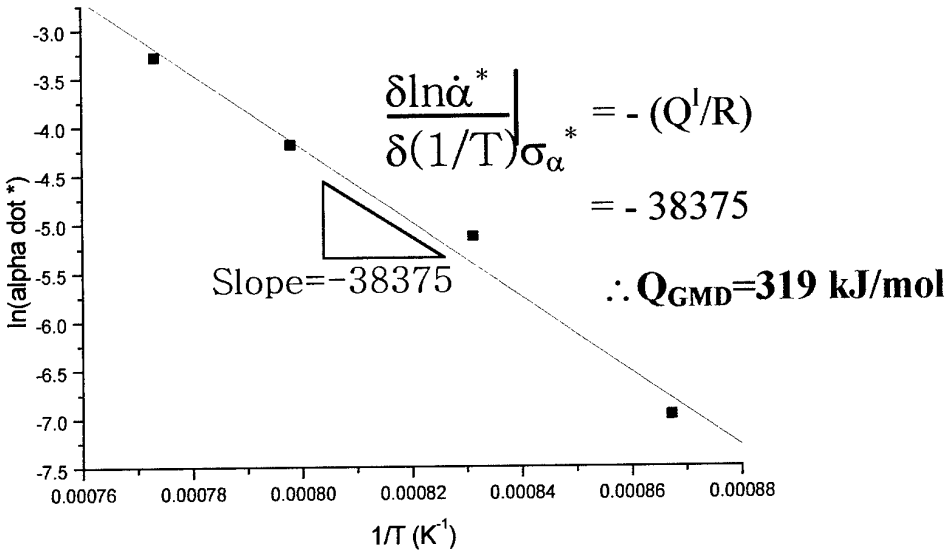

Fig. 33 Temperature dependence of $\dot{\alpha}^*$ in grain matrix deformation

For dislocation climb process, one of the important feature is that the rate-controlling process is the diffusive motion of atoms or vacancies [46-48], rather than the activated glide of the dislocation itself. It is the slowest moving species that is generally believed to be the rate-controlling process. In this study, activation energy for dislocation climb is found to be similar to that for self-diffusion of Al which are 357 kJ/mol in TiAl and 392 kJ/mol in Ti_3Al [61].

6.3. Influence of α_2/γ volume ratio on deformation behavior

The constitutive parameters listed in Table 3 show that the internal strength (σ_α^*) of 5% α_2 volume fraction is higher than that of 30% α_2 phase volume fraction, while reference strain rates $\dot{\alpha}^*$ shows opposite trend. As a result, the flow stress for GMD at a fixed strain rate increases while strain rate for GMD at a fixed stress decreases as the volume fraction of α_2-phase increases. It is suggested that the increase in the flow stress for grain matrix deformation result from the higher hardness of α_2- phase as compared to that of γ phase[9]. Furthermore, since self-diffusion activation energy of Ti and Al in α_2 phase is higher than that in γ phase, dislocation movement in this phase is believed to be more difficult. Thus, total elongation has been reduced with the increase of α2-phase volume fraction as shown in Fig.24. However, in contrast to TiAl alloy, σ^* and $\dot{\alpha}^*$ obtained in Ti-6Al-4V alloy showed reverse tendency. σ^* value is lower and $\dot{\alpha}^*$ value is higher in the 48% β volume fraction microstructure than 28% β microstructure . Thus max elongation is obtained at that microstructure condition.

For the dislocation climb process, $\dot{\beta}^*$ represents a higher value in the 30%-α_2 alloy. Correspondingly the dislocation climb curve shifts to the faster strain rate region at fixed stress level. It is not clearly understood why dislocation climb rate is faster in 30%-α_2 alloy in spite of the slower diffusion rate in α_2 phase. It can be proposed that dislocation emission rate at α_2/γ boundary is faster than at γ/γ boundary. To clarify this mechanism, a more detailed microstructural analysis is required.

6.4. Different cavity initiation probability at γ/γ and α_2/γ boundary

To examine the effect of different boundaries on cavity initiation, microstructures after the tensile deformation have been carefully analyzed. Table 4 shows the tendency of cavity initiation at γ/γ and α_2/γ boundaries. Actually larger numbers of cavities are observed at γ/γ boundaries than at α_2/γ boundaries since there are more γ/γ boundaries than α_2/γ boundaries. The α_2/α_2 boundaries are hardly observed due to the small amount of α_2 phase in this specimen. In order to analyze quantitatively the cavity initiation probability at each boundary, the normalized numbers of cavities are calculated by dividing actual numbers of cavities by phase volume fraction. From this calculation, relative probability of cavity initiation at each boundary is obtained and listed in Table 5;

	γ/γ	α_2/γ
Relative probability of cavity initiation	0.119	0.881

Table 5. Relative probability of cavity initiation at each boundary

The Table 5 indicates that the frequency of cavity initiation at α_2/γ is 8 times higher than that of γ/γ. i.e. α_2/γ boundary is more susceptible in the cavity initiation than γ/γ boundary. This result is well agreed with that shown in Fig.24, in which the total elongation is reduced with increasing α_2 volume fraction. In fact, the volume fraction of cavities observed at fractured area of 30%-α_2 alloy is higher than that of the 5%-α_2 alloy. From TEM micrograph shown in Fig.27 (d), dislocation density in α_2-phase is observed to be much lower than that in γ-phase and the sharp and straight shape of α_2-grain boundary

seems to remain unchanged after large deformation. So, it seems that the amount of deformation of α_2-phase is much lower than that of γ-phase. Thus, there the concentration of misfit strain at α_2/γ boundaries caused the nucleation of microvoid, which would develop the formation of cavities at the boundaries.

7. Summary

In this study, it is aimed to investigate the high temperature deformation mechanisms of two-phase gamma TiAl alloy in view of the inelastic deformation theory. Also, the influence of γ/α_2 volume fraction on high temperature deformation has been analyzed with a special attention to the cavity initiation sites. For this purpose, a series of load relaxation and tensile tests have been conducted at temperature ranging from 800 to 1050°C.

1. In the early stage of the deformation, flow curves of the fine-grained TiAl alloy are well agreed with the combined curves of grain matrix deformation and dislocation climb mechanisms and the evidence of grain boundary sliding has not been observed either in the optical micrographs or in the analysis of load-relaxation tests. With the increase of strain, dynamic recrystallization takes place resulting in the grain refinement, which made GBS become dominant. At the large deformation, flow curves are well matched with the combined curves of grain matrix deformation and grain boundary sliding.

2. The activation energy values for grain matrix deformation and dislocation climb have been obtained from constitutive parameters analysis. The calculated Q_{GMD} is 319kJ/mol, approximately equal to the average value of self-diffusion energy of Ti and Al. This shows that GMD is largely affected by the diffusion of Ti and Al. $Q_{disl.\ climb}$ has been calculated as 386 kJ/mol that is similar to that for self-diffusion of Al (357 kJ/mol in TiAl and 392 kJ/mol in Ti_3Al). Thus, it is suggested that the rate-controlling

process of dislocation climb is diffusive motion of Al atoms.

3. With the increase of α_2-phase volume fraction, the flow stress for GMD at fixed strain rate has been increased presumably due to the higher hardness of α_2- phase as compared to γ phase and higher self-diffusion energy of Ti and Al in α_2-phase. Correspondingly, the total elongation decreases with the increase of α_2-phase volume fraction. Also, the strain rate for dislocation climb at fixed stress level increases as the volume fraction of α_2-phase increases, implying that dislocation emission rate at α_2/γ boundary is faster than at γ/γ boundary. It remains for further investigation.

3. The analysis of normalized numbers of cavities shows that the frequency of cavity initiation at α_2/γ is 8 times higher than that of γ/γ, implying that the α_2/γ boundary is more susceptible sites for cavity initiation than the γ/γ boundary.

8. References

1. J.B.McAndrew and H.D.Kessler: *J.Met.*, 1956,vol.8, pp. 1348-54.
2. S.C.Huang and J.H.Westbrook and R.L.Flesiher, eds., John Wiley & Sons, New York, NY, 1994, pp. 73-90.
3. S.L. Semiatin, D.C. Vollmer, S. El-Soudani, and C. Su, *Scripta Metall. Mater.*, 25, (1991) pp. 1409.
4. H.E. Deve, A.G. Evans and D.S. Shih, *Acta Metall. Mater.*, 40, (1992) pp. 1259.
5. Soboyejo, S.J. Midea, D.S. Schwartz and M.J. Parzuchowski, *Microstructure-Property Relationships in Titanium Aluminides and Alloys*, edited by Y.-W. Kim and R.R. Boyer, TMS, Warrendale, PA (1991) pp. 197.
6. Seetharaman and S.L. Semiatin, *Metall. Trans. A*, 14A, (1996) pp. 1987.
7. Semiatin, V. Seetharaman and I. Weiss, *Mat. Sci. and Eng.* A243, (1998) pp. 1.
8. W.B.Lee, H.S.Yang, Y-W.Kim and A.K.Mukherjee, *Scripta metallurgica.* 29, (1993) pp.1403-1408.
9. Kei Ameyama, Akihiro Miyazaki and Masaharu Tokizane, *Superplasticity in Advanced Materials*, (1991) pp. 317-322.
10. T.Tsuzuku and H.Sato, *Journal de Physique IV*, 3,(1993) pp.389-395
11. N.Ridley, M.F.Islam and Pilling, *Structural Intermetallics*, edited by R.Daralia, J.J. Lewandowski, TMS, (1993) pp. 63-68.
12. M.F.Bartholomeusz, Q.Yang, and J.A.Wert, *Scripta Metal.Mater.*, 29, (1993) pp. 389-94.
13. J.Sun, J.S.Wu, *Journal of Materials science*, 35, (2000) pp. 4919-4922.
14. Takashi Maeda, Minoru Okada and Yoshiaki Shida, *Superplasticity in Advanced Materials*, (1991) pp 311-316.

15. Ji.Sik. Kim ,Young won. Chang, Chongsoo Lee, *Metallurgical and Materials Transactions A*, 29A, (1998) pp. 217-226.

16. A.Dutta and D.Banerjee, *Scripta Metall.*, 24, (1990), pp 1319.

17. T.G. Langdon : *Mater. Sci. and Eng.*, A174, (1994), pp. 225.

18. Z.R. Lin, A.H. Chokshi and T.G. Langdon, *J. of Mater. Sci.*, 23, (1988), pp. 2712.

19. Y.W. Chang and E.C. Aifantis, *Constitutive Laws for Engineering Materials; Theory and Application*, edited by C.S. Desai, (1987), pp. 293.

20. Lipsitt, H.A, *Mater.Res.Soc.Symp.Proc.*, 39 ,(1985), pp.351

21. E.S.Bumps, H.D.Kessler and M.Hansen, *Trans.TMS-AIME*, 194, (1952), pp.609-614

22. P.Duwez and J.L.Taylor, *JOM*, (January 1952), p.70.

23. S.C.Huang, E.L.Hall and M.F.X. Gigliotti, *High-Temperature Ordered Intermetallic Alloys II,* ed. N.S.Stoloff et al. (Pittsburgh, PA:MRS, 1987), pp.481-486.

24. J.H.Perepezko et al, *High Temperature Aluminide & Intermetallics*, ed. S.H.Whang et al. (Warrendale, PA:TMS, 1990), pp.19-47

25. D.S.Lee, A.G.Jackson and J.Menon, unpublished results (1991)

26. S-C.Huang and D.S.Shih, *Microstructural Property Relationships in Titanium Aluminides and Alloys*, ed. Y-W.Kim and R.R.Boyer (TMS), (1991), pp.105-122.

27. S.Tsuyama, S.Mitao and K.Minakawa, *Microstructural Property Relationships,* pp.297-312.

28. T.Tsujimoto and R.Hashimoto, op.cit. 16, pp.391-396.

29. Y-W.Kim, *High-Temperature Ordered Intermetallic Alloys IV*, ed. J.O.Stiegler, L.A.Johnson and D.P.Pope (Pittsburgh, PA:MRS,1991), pp.777-794.

30. Y-W.Kim and F.H.Froes, *High Temperature Aluminide & Intermetallics*, ed. S.H.Whang et al. (Warrendale, PA:TMS, 1990), pp.465-492.

31. D.Shechtman, M.J.Blackburn and H.A.Lipsitt, *Met.Trans.*, 5(june 1974), p.1373.

32. G.Hug, A.Loiseau and A.lasalmonie, *Phil.Mag.A*, 57(3) (1986), pp. 47-65.

33. H.A.Lipsitt, D.Shechtman and R.E.Schafrik, *Met.Trans.A*, 6A (1975). P.1991.

34. E.L.Hall and S.C.Huang, op.cit. 16, pp.693-698.

35. W.T.Donlon, W.E.Dowling, Jr. and J.E.Allison, op.cit. 14, pp.75-90.

36. Y-W.Kim and Dennis M.Dimiduk, *JOM*, (August 1991), pp.40-47.

37. Huang,S.C. and Siemers, *Metall. Trans.*, 20A (1989), pp. 1899.

38. A.K.Gosh and R.A.Ayres, *Metall.Trans*, 7A (1976), pp.1589.

39. N.E.Paton and C.H.Hamilton, *Metall.Trans*, 10A (1979), pp.241

40. D.Grivas, J.W.Morris Jr. and T.G.Langdon, *Scripta Metall*, 15 (1981), pp.229.

41. A.Arieli and A.K.Mukherjee, *Scripta Metall.* 15 (1981), pp.237.

42. A.Aran, *Scripta Metall*, 13 (1979), pp.843.

43. A.E.Geckinli, *Met.Sci.* 17 (1983), pp.12.

44. Sakai and Jonas, *Dynamic Recrystallization*, pp.190-209.

45. William Roberts, *Deformation, Processing and Structure.* Papers presented at the 1982 ASM Materials Science Seminar, pp.109-184.

46. Weertman.J, *J.Mech.Phys.Solid*, 4 (1956), pp.230.

47. Weertman.J, *Trans.AIME*, 218 (1960), pp.207

48. Weertman.J,, *Trans.AIME*, 227 (1963), pp.1475.

49. Padmanabhan, K.A. and Davis.G.J, *Superplasticity.* Springer-Verlag. Berlin, Germany, 1980.

50. Sherby, O.D. and Wadsworth, J., *Prog.Mater.Sci.*, 33 (1989), pp.169.

51. Edington, J, W., Melton, K. N. and Cutler, C.P., *Prog.Mater.Sci.*, 21 (1976), pp.61.

52. Hall, D. and Bacon, D.J., *Int. Dislocations*. Pergamon Press, 1983, pp.168.

53. Hart, E.W., *J.Engng Master.Tech.*,106 (1984), pp.322.

54. Ha.T.K. and Chang.Y.W., *Scripta mater.*, 35 (1996), pp.1317.

55. Hart, E.W., *Stress Relaxation Testing*, ed.A. Fox. ASTM Special Technical Pub. No.676. Baltimore.MD, 1979. pp.5.

56. Enrique. R and Gillis.P.P, *Metall.Trans.*, 22A (1991), pp.2302.

57. Lee, D. and Hart, E. W., *Metall. Trans.*, 2A (1971), pp.1245.

58. R.Gnanamoorthy, Y.Mutoh, and Y.Mizuhara: *Mater.Sci.Eng. A197*, (1995), pp. 69-77.

59. Sung,H.J., Kim,K.S. and Chang,Y.W., *J. Korean .Inst. Metals Mater.*, 31 (1993), pp.48.

60. Ha,T.K. and Chang,Y.W., *Scripta metal.*, 32 (1995), pp.809.

61. Y.Mishin and Chr.Herzig, *Acta Mater*, 48 (2000), pp.589-623.

62. S.W.Schwenker and Y-W.Kim, *Gamma Titanium Aluminides* edited by Y-W.Kim, R.Wagner and M.Yamaguchi TMS, 1995, pp.985.

63. Wonkyu Bang, *Microstructural study on superplasticity deformation behvior of quasi-sing phase alloy*, 1997